

Modeling of Geophysical Flows – Analysis of Models and Modeling Assumptions Using UQ

Ali Akhavan Safaei¹, Andrea Bevilacqua², Abani K. Patra^{1,3}, E. Bruce Pitman⁴, and Marcus I. Bursik²

¹*Dept. of Mech. and Aero. Eng., University at Buffalo, Buffalo NY 14260*

²*Dept. of Geology, University at Buffalo, Buffalo NY 14260*

³*Comp. Data Science and Eng., University at Buffalo, Buffalo NY 14260*

⁴*Dept. of Materials Design and Innovation, University at Buffalo, NY, 14260*

{abani,aliakhav,abevilac,pitman,mib}@buffalo.edu

Abstract

Dense large scale granular avalanches are a complex class of flows with physics that has often been poorly captured by models that are computationally tractable. Sparsity of actual flow data (usually only a posteriori deposit information is available) and large uncertainty in the mechanisms of initiation and flow propagation make the modeling task challenging and a subject of much continuing interest. Models that appear to represent the physics well in certain flows turn out to be poorly behaved in others due to intrinsic mathematical or numerical issues. Nevertheless, given the large implications on life and property many models with different modeling assumptions have been proposed.

While, inverse problems can shed some light on parameter choices it is difficult to make firm judgments on the validity or appropriateness of any single or set of modeling assumptions for a particular target flow or potential flows that needs to be modeled for predictive use in hazard analysis. We will present here an uncertainty quantification based approach to carefully, analyze the effect of modeling assumptions on quantities of interest in simulations based on three established models (Mohr-Coulomb, Pouliquen-Forterre and Voellmy-Salm) and thereby derive a model (from a set of modeling assumptions) suitable for use in a particular context. We also illustrate that a simpler though more restrictive approach is to use a Bayesian modeling average approach based on the limited data to combine the outcomes of different models.

We juxtapose observation data to the simulation results, only with the purpose to maintain a link to the real occurrence of a geophysical flow representing a possible outcome of the case studies described. The fundamental focus of this paper is the exploration of the dynamics of the simulated flows, enabling a notion of the contribution of different mechanisms or models elements inside the simulation procedure, in a fully quantitative, predictive-use oriented and statistical framework.

1 Introduction

1.1 Geophysical mass flows

Geophysical mass flows include debris and mud flows, landslides, snow and rock avalanches, glacier flows, pyroclastic surges, block and ash flows, and pumice flows, lahars, jökulhaups and many other examples. These flows are sometimes tens of kilometers in length and may travel at speeds as fast as hundreds of meters per second. Their deposits can be as much as tens of meters deep and kilometers long. In other words, there is no single universal description of a “typical” geophysical mass flow. Different types of flows are the results of different types of mechanisms/processes and hence different types of flows will have significantly different physical characteristics.

The rheology complexity of the fluidized material, and the mathematical problem of modeling and computing, make the description of the dynamics of those flows really challenging. In many cases the flows are *shallow*, i.e. the horizontal dimension is significantly larger than the flow depth. This assumption allows to perform depth-integration on the governing 3D Navier-Stokes equations, resulting in the 2D formulation of Shallow Water Equations (SWE), also known as Saint Venant Equations (??). Pioneering work of ? that was followed by ?? developed a depth-averaged model for flow of granular materials. Their model was used to model a flow of granular material down an inclined plane, originally using the Mohr-Coulomb rheology (MC) (see also ??). Afterwards, large number of studies focused on the modeling of granular flows, including geophysical mass flows, using SWE approach and many of them were carefully reviewed in ?.

Modeling flow of granular material down an inclined plane was explored in detail by several further studies, both theoretically and experimentally (?????). Granular material slumping (??), rapid flow down smooth inclines (??) and shock waves (??) were modeled and tested. Terrain erosion effects were investigated (??), and also material deposition and self-channeling effects (??).

In particular, the experiments on rough inclined planes led to the development of the Pouliquen-Forsterre rheology (PF), assuming a variable frictional behavior as a function of flow regime (i.e. Froude Number, Fr) and flow depth (????). They allowed for an improved modeling of front propagation, mass spreading, surface wave-propagation and vortices-evolution in the flows on a rough terrain (??).

In parallel to and sometimes anticipating the earth avalanches experiments and models, study of snow avalanches led to the development of the Voellmy-Salm rheology (VS) (????). Dense snow or debris avalanches consist of mobilized, rapidly flowing ice-snow mixed to debris-rock granules (?). The VS rheology assumes a velocity dependent resisting term in addition to the traditional basal friction, ideally capable of including an approximation of the turbulence-generated friction. Many experimental and theoretical studies were developed in this framework (????).

In ?????, the depth-averaged model was further studied and applied in the simulation of geophysical flows over digital models of natural terrains. Moreover, ?? tested modeling of fast avalanches, exploring the high-velocity effects of channelizing/chuting topographies. A compensation for the effect of earth pressure changes was implemented and explored in detail (??), as well as the implementation of a significant curvature in the terrain (??). Several specific studies on the pore pressure effects on the flow initiation and fluidization were developed (??). A two-phase model was also implemented to more accurately simulate heterogenous flows with a significant portion of interstitial fluid (?). All of these complex modeling choices correspond to alternative or additional physical assumptions, and they are sometimes very difficult to be evaluated, compared or reasonably combined together.

A particular interest is raised by the specific efforts devoted to the modeling of volcanic mass flows with SWE (??????????). Volcanoes are great sources for a rich variety of geophysical flow types in addition to the collected field data from past flow events.

In this study, we use TITAN2D software that is a publicly available toolkit for simulation of granular flows over natural terrains by solving depth-averaged equations using Digital Elevation Model (DEM) of terrain (?????). In the 4th release of TITAN2D, the capability of having multiple rheology options (MC, PF and VS rheologies) for simulation of flow in the same computational platform have been implemented. Therefore, we can perfectly make use of this opportunity and only focus on modeling characteristics of these rheology options without concerns about effects of diverse numerical frameworks. So far, TITAN2D achieved many successful applications in the simulation of different geophysical mass flows with specific peculiarities (????????). Several studies involving TITAN2D were recently directed towards a statistical study of geophysical flows, focusing on the uncertainty quantification and propagation (????), or on the

more efficient production of hazard maps (????).

This study for the first time applies a statistical approach to the detailed investigation of the material model *stress components* and their associated *powers*, as well as the *Froude Number Fr*, the *acceleration* and observable quantities as the flow *velocity*, *height*, *lateral extent*, and *area*. The stress components have a strong link with the dynamic equation terms, while *Fr* can give information on the flow regime; moreover, the observable quantities have a direct link to field data and hazard assessments. This can provide a complete description of the geophysical flow. Our main purpose is to obtain a quantitative and statistical understanding of the consequences of the different physical assumptions, both on the forces inside the flow and on the observable outputs in time and space.

In particular, what we present is a procedure for the improved exploration and quantitative comparison of physical models and their assumptions through the collection of full statistical data. Behind each physical model there are different physical assumptions, and therefore it is more appropriate to look at those instead than at the entire model results. Our statistical approach shall enable a first step towards a data driven selection of the best modeling assumptions to use.

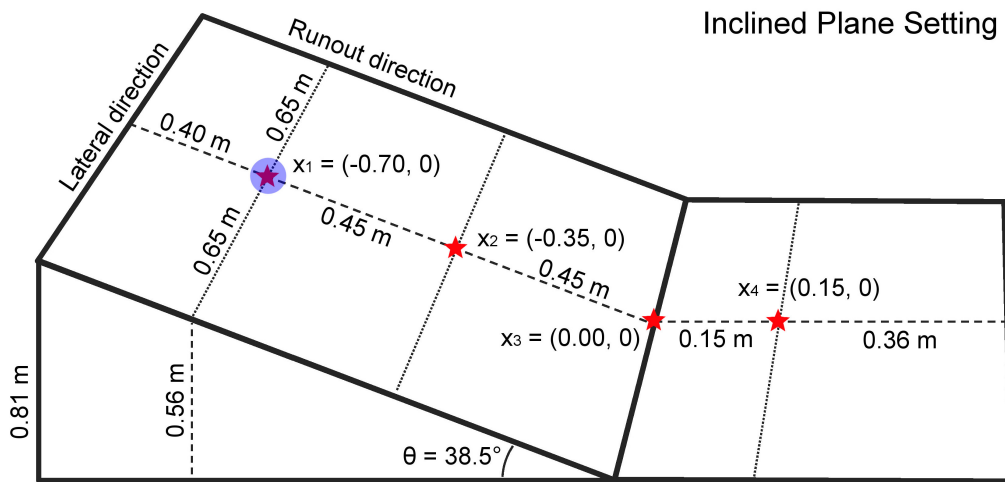


Figure 1: Inclined plane description, including local samples sites (red stars). Pile location is marked by a blue dot.

1.2 Overview of the case studies

The first case study assumes very simple boundary conditions, and corresponds to an experiment fully described in ????. It is a classical flow down an inclined plane set-up, including a change in slope to an horizontal plane (Fig. 1). Four locations are selected among the center line of the flow to accomplish local testing. These are: the initial pile location $L_1 = (-0.7, 0)$ m, the middle of the inclined plane $L_2 = (-0.35, 0)$ m, the change in slope $L_3 = (0, 0)$ m, the middle of the flat plane $L_4 = (0.15, 0)$ m (see Section 4).

The second case study is a block and ash flow down the slope of Volcán de Colima (México) - an andesitic stratovolcano that rises to 3,860 m above sea level, situated in the western portion of the Trans-Mexican Volcanic Belt (Fig. 2). Historically, it has been the most active volcano in México (???). The modeling of pyroclastic flows generated by explosive eruptions and lava dome collapses of Volcán de Colima is a well studied problem (??????). The volcano has been already used as a case study in several research involving the Titan2D code (??????). During July 10th-11th, 2015, the volcano underwent its most intense eruptive phase since its Subplinian-Plinian 1913 AD eruption (????).

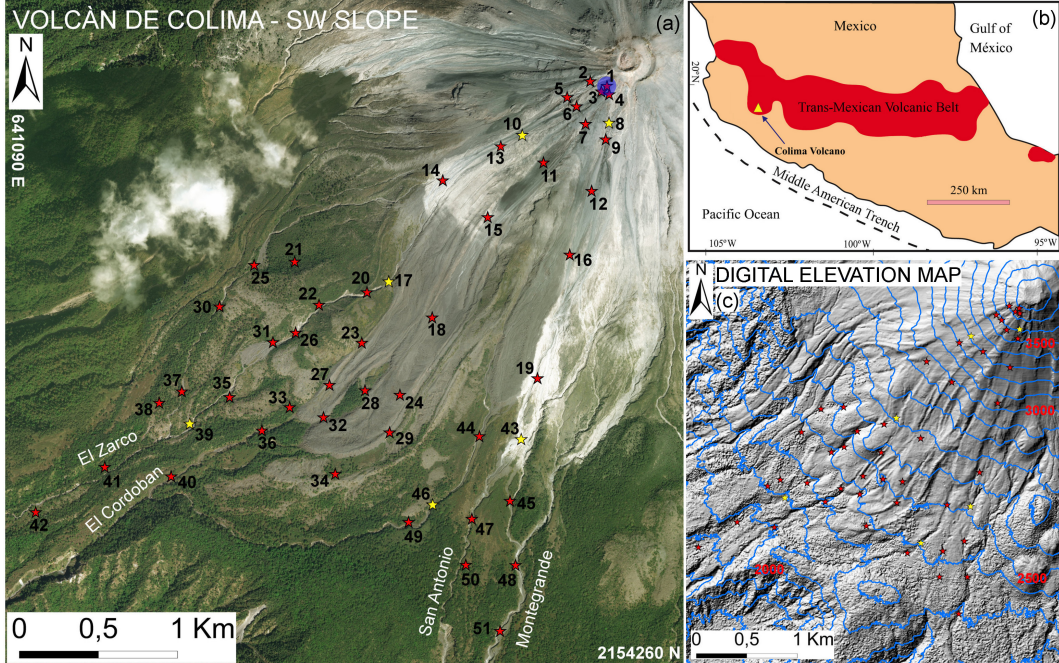


Figure 2: (a) Volcán de Colima (Méjico) overview, including 51 numbered local sample sites (stars) and four labeled major ravines channeling the flow. Pile location is marked by a blue dot. Reported coordinates are in UTM zone 13N. Background is a satellite photo. (b) Regional geology map. (c) Digital elevation map. Six points that are adopted as preferred locations are highlighted in yellow. Elevation isolines are included in blue, elevation values in red.

We assume the flow to be generated by the gravitational collapse of a paraboloid dome placed close to the summit area. A dome collapse occurs when there is a significant amount of recently-extruded highly-viscous lava piled up in an unstable configuration around a vent. Further extrusion and/or external forces can cause the still hot dome of viscous lava to collapse, disintegrate, and avalanche downhill (??). The hot, dense blocks in this “block and ash” flow (BAF) will typically range from centimeters to a few meters in size. The matrix is composed of fine ash from the comminuted blocks. Computations were performed on a DEM with 5m-pixel resolution, obtained from LiDAR data acquired in 2005 (??). We select 51 locations along the flow inundated area to accomplish local testing. Six of them are then adopted as preferred locations, being representative of different flow regimes (see Section 5).

2 Overview of the models

2.1 Modeling Assumptions

The models of geophysical mass flows described in this study rely on several physical and mathematical assumptions. We will classify them in two groups - the general assumptions and the rheology assumptions. The main focus of this study is on the latter group, but, in principle, the same procedure could be applied to the former.

General Assumptions

- The *shallowness* approximation is at the base of the depth-averaging procedure. In this approximation, the flow depth is assumed to be at least an order of magnitude less than the characteristic length of the flowing material. Variation of velocity within the flow depth is neglected.
- The material is assumed to be *continuous*. The real flows consist of granular material and, often, interstitial fluid. Usually the “typical particle” diameter is small compared to the depth and length

of the flowing mass, and the rheological properties are imposed to approximate the bulk behavior that is expected of an actual mass flow.

- The moving mass is assumed to be *volume preserving*. In contrast, phenomena of erosion and deposition of material may violate this assumption.
- The flowing mass is assumed to be consisted of an *incompressible* fluid. This means that we are ignoring variations of density due to the void ratio (i.e. the density is uniform in space and time).
- The body of mass is supposed to be in *isothermal* state or, if not, thermal effects can be ignored.
- The mass flow is assumed to be *free surface*. Air entrainment is instead frequently observed in the dilute real flows.
- The stress tensor is assumed *symmetric* with respect to the z axis.

The shallowness assumption is very important, and brings several implications which may be considered additional assumptions on their own.

Consequences of Shallowness

- The shallowness assumption implies a *hydrostatic* expression for the normal pressure in the direction perpendicular to the basal surface. Moreover, the downslope and cross-slope pressure components are assumed to be varying linearly with the normal pressure component through the flow depth.
- The *boundary layer* where the shearing deformation takes place is collapsed to zero thickness. The sliding and shearing velocity are combined to a single sliding law with a somewhat larger modelled sliding velocity.
- The *lateral shear stresses can be neglected*, compared to the basal shear stresses. Motion of the bulk of mass consists of “shearing within the deforming mass” and “sliding along the basal surface”.

The list rheology assumptions is detailed when the models are presented.

2.2 Governing Equations and Boundary Conditions

The motion of the mass flow is described by the basic conservation of mass and momentum for an incompressible medium:

$$\begin{aligned} \nabla \cdot \underline{\mathbf{u}} &= 0, \\ \frac{\partial}{\partial t}(\rho \underline{\mathbf{u}}) + \nabla \cdot (\rho \underline{\mathbf{u}} \otimes \underline{\mathbf{u}}) &= \nabla \cdot \underline{\underline{\mathbf{T}}} + \rho \underline{\mathbf{g}}, \end{aligned} \quad (1)$$

Where $\underline{\mathbf{u}} = [u, v, w]^T$ is the material velocity in cartesian coordinates, ρ is its constant density, $\underline{\underline{\mathbf{T}}}$ is the *Cauchy* stress tensor, and $\underline{\mathbf{g}}$ is the gravity acceleration vector.

The Cauchy stress tensor, $\underline{\underline{\mathbf{T}}}$, depends on the rheology assumptions. The kinetic boundary conditions are defined on the free surface $F^s = s(x, y, t) - z = 0$ and basal surface $F^b = b(x, y, t) - z = 0$ interfaces:

$$\frac{\partial F^s}{\partial t} + \underline{\mathbf{u}} \cdot \nabla F^s = 0, \quad \text{at } F^s(x, y, t) = 0 \quad (2)$$

$$\frac{\partial F^b}{\partial t} + \underline{\mathbf{u}} \cdot \nabla F^b = 0, \quad \text{at } F^b(x, y, t) = 0 \quad (3)$$

The depth-averaged Saint-Venant equations that TITAN2D solves are:

$$\begin{aligned} \frac{\partial h}{\partial t} + \frac{\partial}{\partial x}(h\bar{u}) + \frac{\partial}{\partial y}(h\bar{v}) &= 0, \\ \frac{\partial}{\partial t}(h\bar{u}) + \frac{\partial}{\partial x}\left(h\bar{u}^2 + \frac{1}{2}kg_z h^2\right) + \frac{\partial}{\partial y}(h\bar{u}\bar{v}) &= S_x, \\ \frac{\partial}{\partial t}(h\bar{v}) + \frac{\partial}{\partial x}(h\bar{u}\bar{v}) + \frac{\partial}{\partial y}\left(h\bar{v}^2 + \frac{1}{2}kg_z h^2\right) &= S_y \end{aligned} \quad (4)$$

Here the cartesian coordinate system is aligned such that z is normal to the surface; h is the flow height in the z direction; $h\bar{u}$ and $h\bar{v}$ are respectively the components of momentum in the x and y directions; and k

is the coefficient which relates the lateral stress components, $\bar{\sigma}_{xx}$ and $\bar{\sigma}_{yy}$, to the normal stress component, $\bar{\sigma}_{zz}$. The definition of this coefficient depends on the constitutive model of the flowing material we choose. Note that $\frac{1}{2}kg_z h^2$ is the contribution of hydrostatic pressure to the momentum fluxes. S_x and S_y are the sum local stresses: they include the gravitational driving forces, the basal friction force resisting to the motion of the material, and additional forces specific of rheology assumptions.

2.2.1 Numerical solver

Let $\mathbf{U} = [h, h\bar{u}, h\bar{v}]^T$ be the vector of conservative variables and $\mathbf{F} = [h\bar{u}, h\bar{u}^2 + 0.5k_{ap}g_z h^2, h\bar{v}\bar{u}]^T$ and $\mathbf{G} = [h\bar{v}, h\bar{u}\bar{v}, h\bar{v}^2 + 0.5k_{ap}g_z h^2]^T$ be the physical flux vectors. In order to solve the system of hyperbolic conservation laws (4), TITAN2D employs a finite volume Godunov solver, and the time-stepping procedure is achieved by an explicit Euler scheme (??). Assuming $\mathbf{S} = [S_h, S_x, S_y]^T$ as the source terms vector containing the effect of the flow rheology, the flow in the next time step updates as:

$$\mathbf{U}_{i,j}^{n+1} = \mathbf{U}_{i,j}^n - \frac{\Delta t}{\Delta x} \{ \mathbf{F}_{i+\frac{1}{2},j}^n - \mathbf{F}_{i-\frac{1}{2},j}^n \} - \frac{\Delta t}{\Delta y} \{ \mathbf{G}_{i,j+\frac{1}{2}}^n - \mathbf{G}_{i,j-\frac{1}{2}}^n \} + \Delta t \, \mathbf{S}_{i,j} \quad (5)$$

Where $\mathbf{F}_{i\pm\frac{1}{2},j}^n$ and $\mathbf{G}_{i,j\pm\frac{1}{2}}^n$ are the numerical flux terms at the inter-cell boundaries which are computed regarding the Harten-Lax-Van Leer Riemann solver (?) . In fact, the evolution of the flow to the next time step depends on the advection flux at the cell interface, which results from the wave interaction at the boundaries between cells. On the other hand, adaptive mesh refinement allows for the concentration of computing power on regions of special interest. It captures the complex flow features along the flow boundaries, as well as the locations where there are large mass or momentum fluxes (which may include places where the topography changes abruptly). Mesh coarsening is also applied where the solution values are relatively constant or small to further improve the computational efficiency (??).

2.3 Rheology assumptions

In the three following sections, we briefly describe *Mohr-Coulomb* (MC), *Pouliquen-Forterre* (PF) and *Voellmy-Salm* (VS) models.

2.3.1 Mohr-Coulomb model

Based on the long history of studies in soil mechanics (?), the Mohr-Coulomb rheology model was developed and used to represent the behavior of geophysical mass flows ?.

Shear and normal stress are assumed to obey Coulomb friction equation, both within the flow and at its boundaries. In other words,

$$\tau = \sigma \tan \phi, \quad (6)$$

where τ and σ are respectively the shear and normal stresses on failure surfaces, and ϕ is a friction angle. This relationship does not depend on the flow speed.

Under the assumption of symmetry of the stress tensor w.r.t. the z axis, the earth pressure coefficient $k = k_{ap}$ can take on only one of three values indicated by the square dots shown in Figure 3. The material yield criterion is represented by the two straight lines at angles $\pm\phi$ (the internal friction angle) relative to horizontal direction. Similarly, the normal and shear stress at the bed are represented by the line $\tau = -\sigma \tan(\delta)$ where δ is the bed friction angle. The three possible stress states in the xz -plane are indicated by the square dots. The circular dots show the additional possible stress states for σ_{yy} for a non-axisymmetric stress tensor.

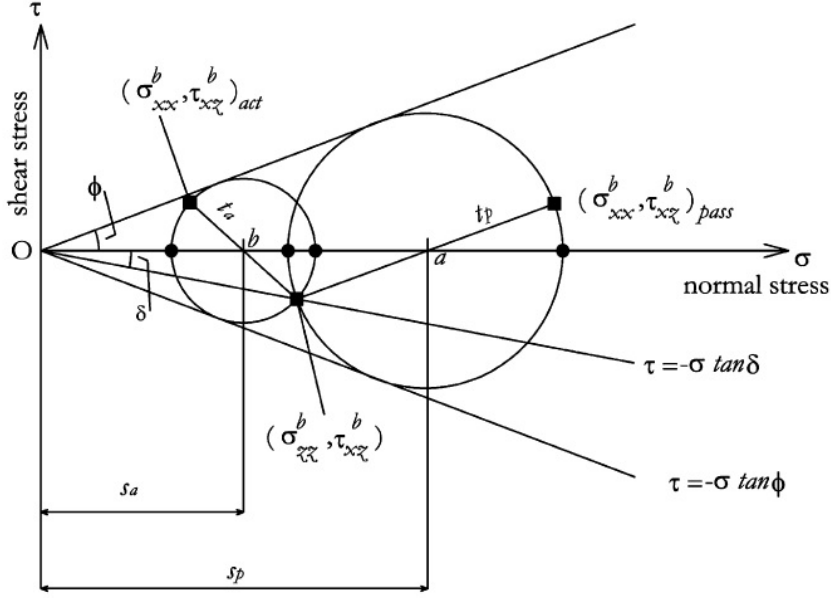


Figure 3: Mohr-circle-diagram representing the stress state within a granular medium (?).

Regarding the friction angle stated above, we have two material properties in this model:

- Internal friction angle, ϕ_{int} , which resists material shear.
- Bed friction angle, ϕ_{bed} , which resists motion of the material relative to the bed. This is a joint property of the material and the surface it flows over.

It is worth mentioning that the effective value of the friction angles can be strongly reduced by the presence of interstitial fluid, sometimes creating modeling issues. Specific models have been developed in case the effect of interstitial fluid is believed to be particularly relevant (?).

Earth pressure coefficient $k = k_{ap}$ is defined in MC as:

$$k_{ap} = \begin{cases} \frac{\sigma_{xx}^{b\ act}}{\sigma_{zz}^b} = 2 \frac{1 - \sqrt{1 - \cos^2(\phi_{int})(1 + \tan^2(\phi_{bed}))}}{\cos^2(\phi_{int})} - 1, & \nabla \cdot \tilde{\mathbf{u}} > 0, \text{ active} \\ \frac{\sigma_{xx}^b}{\sigma_{zz}^b} = 1, & \nabla \cdot \tilde{\mathbf{u}} = 0, \text{ neutral} \\ \frac{\sigma_{xx}^{b\ pass}}{\sigma_{zz}^b} = 2 \frac{1 + \sqrt{1 - \cos^2(\phi_{int})(1 + \tan^2(\phi_{bed}))}}{\cos^2(\phi_{int})} - 1, & \nabla \cdot \tilde{\mathbf{u}} < 0, \text{ passive} \end{cases} \quad (7)$$

MC equations As a result, we can write down the source terms of the Eqs. (4):

$$\begin{aligned} S_x &= g_x h - \frac{\bar{u}}{\|\tilde{\mathbf{u}}\|} \left[h \left(g_z + \frac{\bar{u}^2}{r_x} \right) \tan(\phi_{bed}) \right] - h k_{ap} \operatorname{sgn} \left(\frac{\partial \bar{u}}{\partial y} \right) \frac{\partial(g_z h)}{\partial y} \sin(\phi_{int}), \\ S_y &= g_y h - \frac{\bar{v}}{\|\tilde{\mathbf{u}}\|} \left[h \left(g_z + \frac{\bar{v}^2}{r_y} \right) \tan(\phi_{bed}) \right] - h k_{ap} \operatorname{sgn} \left(\frac{\partial \bar{v}}{\partial x} \right) \frac{\partial(g_z h)}{\partial x} \sin(\phi_{int}) \end{aligned} \quad (8)$$

Where, $\tilde{\mathbf{u}} = (\bar{u}, \bar{v})$, is the depth-averaged velocity vector, r_x and r_y denote the radii of curvature of the local basal surface. The inverse of the radii of curvature is usually approximated with the partial derivatives of the basal slope, e.g., $1/r_x = \partial \theta_x / \partial x$, where θ_x is the local bed slope.

MC rheology assumptions In summary:

- *Basal Friction* is based on a constant friction angle.
- *Internal Friction* gives a not negligible contribution and it is based on a constant friction angle.
- *Earth pressure coefficient* formula depends on the Mohr-Coulomb circle.
- Velocity based *curvature effects* are included into the equations.

2.3.2 Pouliquen-Forterre model

The scaling properties for granular flows down rough inclined planes led to a new formulation of the basal friction stress as a function of the flow depth and velocity (?).

Two critical slope inclination angles are defined as functions of the flow thickness, namely $\phi_{start}(h)$ and $\phi_{stop}(h)$. The function $\phi_{stop}(h)$ gives the slope angle at which a steady uniform flow leaves a deposit of thickness h , while $\phi_{start}(h)$ is the angle at which a layer of thickness h is mobilized. They define two different basal friction coefficients:

$$\mu_{start}(h) = \tan(\phi_{start}(h)) \quad (9)$$

$$\mu_{stop}(h) = \tan(\phi_{stop}(h)) \quad (10)$$

An empirical friction law $\mu_b(\|\tilde{\mathbf{u}}\|, h)$ is then defined in the whole range of velocity and thickness. The expression changes depending on two flow regimes, according to a parameter β and the Froude number $Fr = \|\tilde{\mathbf{u}}\| / \sqrt{hg_z}$.

Dynamic friction regime - $Fr \geq \beta$

$$\mu(h, Fr) = \mu_{stop}(h\beta/Fr) \quad (11)$$

Intermediate friction regime - $0 \leq Fr < \beta$

$$\mu(h, Fr) = \left(\frac{Fr}{\beta} \right)^\gamma [\mu_{stop}(h) - \mu_{start}(h)] + \mu_{start}(h), \quad (12)$$

where γ is the power of extrapolation, assumed equal to 10^{-3} in the sequel (?). In particular, if $Fr = \beta$, then $\mu(h, Fr) = \mu_{stop}(h)$, and if $Fr = 0$, then $\mu(h, Fr) = \mu_{start}(h)$.

The functions μ_{stop} and μ_{start} are defined by:

$$\mu_{stop}(h) = \tan \phi_1 + \frac{\tan \phi_2 - \tan \phi_1}{1 + h/\mathcal{L}} \quad (13)$$

and

$$\mu_{start}(h) = \tan \phi_3 + \frac{\tan \phi_2 - \tan \phi_1}{1 + h/\mathcal{L}} \quad (14)$$

The critical angles ϕ_1 , ϕ_2 and ϕ_3 and the parameters \mathcal{L}, β are the parameters of the model.

In particular, \mathcal{L} is the characteristic depth of the flow over which a transition between the angles ϕ_1 to ϕ_2 occurs, in the μ_{stop} formula. In practice, if $h \ll \mathcal{L}$, then $\mu_{stop}(h) \approx \tan \phi_2$, and if $h \gg \mathcal{L}$, then $\mu_{stop}(h) \approx \tan \phi_1$. The effect of the topographic local curvatures is also taken into account.

PF equations The depth-averaged Eqs. (4) source terms thus take the following form:

$$\begin{aligned} S_x &= g_x h - \frac{\bar{u}}{\|\tilde{\mathbf{u}}\|} \left[h \left(g_z + \frac{\bar{u}^2}{r_x} \right) \mu_b(\|\tilde{\mathbf{u}}\|, h) \right] + g_z h \frac{\partial h}{\partial x} \\ S_y &= g_y h - \frac{\bar{v}}{\|\tilde{\mathbf{u}}\|} \left[h \left(g_z + \frac{\bar{v}^2}{r_y} \right) \mu_b(\|\tilde{\mathbf{u}}\|, h) \right] + g_z h \frac{\partial h}{\partial y} \end{aligned} \quad (15)$$

PF rheology assumptions In summary:

- *Basal Friction* is based on an interpolation of different friction angles, based on the flow regime and depth.
- *Internal Friction* is neglected.
- *Earth pressure coefficient* is equal to one.
- Normal stress is modified by a *hydrostatic pressure force* related to the flow height gradient.
- Velocity based *curvature effects* are included into the equations.

2.3.3 Voellmy-Salm model

The theoretical analysis of dense snow avalanches led to the VS rheology model (??). The following relation between shear and normal stresses holds:

$$\tau = \mu\sigma + \frac{\rho\|\underline{\mathbf{g}}\|}{\xi}\|\tilde{\mathbf{u}}\|^2, \quad (16)$$

where, σ denotes the normal stress at the bottom of the fluid layer and $\underline{\mathbf{g}} = (g_x, g_y, g_z)$ represents the gravity vector. The VS rheology adds a velocity dependent *turbulent* friction to the traditional velocity independent basal friction term which is proportional to the normal stress at the flow bottom. The two parameters of the model are the bed friction coefficient μ and the turbulent friction coefficient ξ . By dimension analysis, ξ is equivalent to an acceleration, while μ is dimensionless. The decomposition of the total basal friction into velocity independent and dependent parts allows the modeling of either the dynamic regime when the avalanche is flowing with a high velocity in the acceleration zone, and when it is close to stopping in the runout zone.

The effect of the topographic local curvatures is again taken into account by adding the terms containing the local radii of curvature r_x and r_y . In this case the formula is considering the modulus of velocity instead than the scalar component (?).

VS equations Therefore, the final source terms take the following form:

$$\begin{aligned} S_x &= g_x h - \frac{\bar{u}}{\|\tilde{\mathbf{u}}\|} \left[h \left(g_z + \frac{\|\tilde{\mathbf{u}}\|^2}{r_x} \right) \mu + \frac{\|\underline{\mathbf{g}}\|}{\xi} \|\tilde{\mathbf{u}}\|^2 \right], \\ S_y &= g_y h - \frac{\bar{v}}{\|\tilde{\mathbf{u}}\|} \left[h \left(g_z + \frac{\|\tilde{\mathbf{u}}\|^2}{r_y} \right) \mu + \frac{\|\underline{\mathbf{g}}\|}{\xi} \|\tilde{\mathbf{u}}\|^2 \right]. \end{aligned} \quad (17)$$

VS rheology assumptions In summary:

- *Basal Friction* is based on a constant coefficient, similarly to the MC rheology.
- *Internal Friction* is neglected.
- *Earth pressure coefficient* is equal to one.
- Additional *turbulent friction* is based on the local velocity by a quadratic expression.
- Velocity based *curvature effects* are included into the equations, following an alternative formulation.

3 UQ Process

The key to a good forecasting capability in the context of mass flows requires the careful selection of the pair $(M(A), P_{M(A)})$, where A is a set of assumptions, $M(A)$ is the model which combines those assumptions, and P_M is a probability distribution in the parameter space of M . For the sake of simplicity we are always taking P_M uniformly distributed on selected parameter ranges.

Models and assumptions An assumption is a quite general concept - for example it can be a specific equation for the internal stress, the implementation of bed curvature effects, of active-passive material stretching, or the use of a specific correction on the pressure effects. Assumptions are what makes the models being different, and each model may be seen as the combined result of a set of assumptions. Sometimes a good model contains a useless assumption that may be removed, sometimes a good assumption should be implemented inside a different model - those are usually considered as subjective choices, not data driven. Moreover, the correct assumptions may change through time, making the analysis more difficult. We provided a list of assumptions behind SWE general implementation, and behind each rheology in section 2.

Parameters ranges It is worth mentioning that whereas the support of P_M can be restricted to a single point in case an inverse problem is solved for the optimal reconstruction of a particular flow, this is not possible if we are interested in the general predictive capabilities of the model, i.e. the target of probabilistic hazard assessment. In this study we always assume $P_M \sim \bigotimes_{i=1}^{N_M} Unif(a_{i,M}, b_{i,M})$, where N_M is the number of parameters of M . These parameter ranges will not be selected under the influence of a particular observation, but we will try to use the information gathered in literature about the physical meaning of those values, together with a preliminary testing, coupling the range of possible runouts. This coupling step is detailed in section 3.3, and required to focus the statistical comparison on a consistence range of flow regimes.

Simulated quantities The simulation algorithms can be schematized as:

(1) INPUT VARIABLES → (2) HIDDEN DYNAMIC QUANTITIES → (3) OBSERVABLE OUTPUTS

The *input variables* are the parameters of M , i.e. volume, rheology coefficients, but can include also the initiation site and geometry, and the digital elevation map. The *hidden quantities* include the stress terms in the Newton Equations that rule the simulation, and their powers. Those are hidden to the observation in a real flow, but they directly depend on the parameters, and represent a fundamental link between the parameters and the observable outputs. Moreover, the models share some of those terms while change others, and this enables a detailed comparison of the real physics below the curtain (see Sections 4.2, 5.3). Finally, the *observable outputs* include what can be measured in space and time: e.g. flow height, lateral extent, area, velocity, acceleration, and combined quantities as Fr (see Sections 4.1, 5.2). In the sequel (2) and (3) are also called quantities of interest (QoI).

Local samples and spatial averaging The QoI in the previous scheme which are evolving fields $f(\underline{\mathbf{x}}, t)$ in space-time, can be either *locally sampled* or *spatially averaged* (see sections 4, 5). The spatial averaging is defined by $F(t) = \int_{\mathbb{R}^k} f(\underline{\mathbf{x}}, t) d\underline{\mathbf{x}}$. In the most of the cases $k = 2$, and $d\underline{\mathbf{x}}$ is given by the area of the mesh elements. Sometimes $k = 3$, e.g. concerning speed, and $d\underline{\mathbf{x}}$ is the element of volume corresponding to the mesh elements.

A fundamental part of this research was made possible by the new implementation of a local sampling option in the TITAN2D cyber-infrastructure. In particular, once a set of sample points $(x_i)_{i=1,\dots,N}$ is chosen, each field $f(\underline{\mathbf{x}}, t)$ is calculated as a function of time on the elements of the numerical mesh which are found to contain the $(x_i)_{i=1,\dots,N}$. Exploring differences in time and location enable to constrain the changes in flow regime. Those are really important because if the flow behavior is radically different, then the significance and effects of the assumptions may also change.

Monte Carlo simulation In general, for each QoI, during a Monte Carlo simulation we sample the input variables and obtain a family of temporal graphs on time domains depending on the flow duration. These results are statistically summarized - plotting their expectation, and their 5th and 95th percentiles. In the following, we will detail the considered input variables and quantities of interest for each of our cases study.

Our sampling technique of the input variables is based on the Latin Hypercube Sampling (LHS) idea, and in particular, on the improved space-filling properties of the orthogonal array-based Latin Hypercubes (see Appendix 6). The LHS is performed over $[0, 1]^3$ for the MC and VS input parameters, and $[0, 1]^4$ for PF input parameters (see Section 3.3). Those adimensional samples are homothetically transformed to fill the required intervals.

3.1 Statistical analysis of force contributions

A statistical analysis capable of measuring the contributions of different force components in the rheology models is presented. That is helpful to explore and compare the effects of the assumptions behind some modeling choices, onto the time evolution of the flowing material. Let $(F_i(x, t))_{i=1, \dots, 6}$ be the array of force components, where $x \in \mathbb{R}^2$ is a spatial location, and $t \in T$ is a time instant.

In our case study, $(F_1, F_2) := (\mathbf{LHS}_1, \mathbf{LHS}_2)$, i.e. the left-hand side terms in the momentum equation, while $(F_3, \dots, F_6) := (\mathbf{RHS}_1, \dots, \mathbf{RHS}_4)$ are the right-hand side terms. These forces can take different formulations in the different models, which are detailed in section 3.2. This type of procedure can be applied to any additive decomposition of the physical forces. The analysis of RHS can inform on local effects, while LHS concerns the of un-local dynamics in space and time.

In general we show the projection of the forces on the slope direction, or the product with the velocity field, i.e. the power related to them. Hence, in the following the forces are scalar and not vectorial terms. It is important to remark that all the forces are hidden dynamic quantities (see above), depending on the input variables, and they are thus considered as random variables. The degree of contribution of those force terms is significantly variable in space and time, and we define the *contribution coefficients* to model this. The definitions are not depending on the location, but all the results will significantly depend of that choice. Next notation will assume to be in a selected location $x = L_k$, where $k \geq 1$. In the following we will focus on **RHS** forces, although some testing including **LHS** forces has also been accomplished.

Definition 1 (Contribution coefficients) *Let $(F_i)_{i \in I}$ be random variables on (Ω, \mathcal{F}, P) , representing the considered force components in location x at time t . Then, for each component i , the contribution coefficient is defined as:*

$$C_i := \mathbb{E} \left[\frac{F_i}{\Phi} \right],$$

where Φ is a dominating function, i.e. $\Phi \geq |F_i|, \forall i \in I$.

The *total force*, i.e. $\sum_i F_i$ excluding the inertial terms, is not a good candidate for a dominating function. Indeed, the terms often have opposite signs, and their sum can be really small. Another issue is given by the existence of a subset of times Θ characterized by the absence of flow in the selected location x . In Θ the dominant force is null, and cannot be the denominator of a fraction.

We have tested two alternative Φ choices: Φ_1 is based on the l^1 norm, and defined as:

$$\Phi_1 := \begin{cases} \sum_i \frac{|F_i|}{2}, & \text{if not null;} \\ 1, & \text{otherwise.} \end{cases}$$

In contrast Φ_2 is a dominant force based on the l^∞ norm:

$$\Phi_2 := \begin{cases} \max_i |F_i|, & \text{if not null;} \\ 1, & \text{otherwise.} \end{cases}$$

In particular, for a particular location x , time t , and parameter sample ω , we have $C_i = 0$ if there is no flow or all the forces are null. The expectation of C_i is reduced by the chance of F_i being small compared to the other terms, or by the chance of having no flow in (x, t) . Moreover, $\mathbb{E}[C_i] \in [-1, 1], \forall i$.

Proposition 2 *Let $\Phi_k, k = 1, 2$ be the functions described above. Then they are well defined dominating function, i.e. $\Phi_k \geq |F_j|, \forall j, k$.*

Proof. If $k = 1$, the Newton equation states $\sum_{j \in J} F_j = \sum_{i \in I} F_i$, where $(F_j)_{j \in J}$ are inertial forces, and $(F_i)_{i \in I}$ the local forces. Then, $\forall h \in I$

$$F_h = \sum_{i \neq h, i \in I} F_i - \sum_{j \in J} F_j.$$

And hence

$$|F_h| \leq |F_h| + \sum_{i \neq h, i \in I} |F_i| - \sum_{j \in J} |F_j| = 2\Phi_1.$$

A similar equation is valid $\forall k \in J$. If $k = 2$, or if the inertial forces are not included, the proof is trivial. \square

Furthermore, assuming $\Phi = \Phi_2$, there is a useful result explaining the meaning of those coefficients through the conditional expectation.

Proposition 3 Let $(F_i)_{i \in I}$ be random variables on (Ω, \mathcal{F}, P) , representing the considered force components in location x at time t . For each i , let C_i be the contribution coefficient of force F_i , assuming $\Phi = \Phi_2$. Then we have the following expression:

$$C_i = \sum_j p_j \mathbb{E} \left[\frac{F_i}{|F_j|} \mid \Phi = |F_j| \right],$$

where $p_j := P \{ \Phi = |F_j| \}$.

Proof. Let Z be a discrete random variable such that, for each $j \in \mathbb{N}$, $(Z = j) \iff (\Phi = |F_j|)$. Then, by the rule of chain expectation:

$$\begin{aligned} C_i &= \mathbb{E} \left[\frac{F_i}{\Phi} \right] = \mathbb{E} \left[\mathbb{E} \left[\frac{F_i}{\Phi} \mid Z = j \right] \right] = \\ &= \mathbb{E} \left[\mathbb{E} \left[\frac{F_i}{|F_j|} \mid Z = j \right] \right] = \sum_j P \{ Z = j \} \mathbb{E} \left[\frac{F_i}{|F_j|} \mid Z = j \right]. \end{aligned}$$

Moreover, by definition, $p_j = P \{ Z = j \}$. This completes the proof. \square

The last proposition brings to the definition of the *dominance factors* $(p_j)_{j=1,\dots,k}$, i.e. the probability of each F_j to be the dominant force in (x, t) .

Definition 4 (Dominance factors and conditional contributions) Let $(F_i)_{i=1,\dots,k}$ be random variables on (Ω, \mathcal{F}, P) , representing arbitrary force components in location x at time t . Then, for each pair of components (i, j) , the conditional contribution $C_{i,j}$ is defined as:

$$C_{i,j} := \mathbb{E} \left[\frac{F_i}{|F_j|} \mid \Phi = |F_j| \right],$$

where $\Phi = \Phi_2$ is the dominant force. In particular, for each component i , the dominance factor is defined as:

$$p_j := P \{ \Phi = |F_j| \}.$$

In sections 4.2.4 and 5.3.4 we display the contribution coefficients as a function of time, assuming $\Phi = \Phi_2$. Moreover, we report the dominance factors plots, another very useful tool to read the dynamic significance of the forces as a function of time and location.

3.2 Forces terms definition

Forces analyzed have been classified according to the terms of the momentum equation in (4). Moreover, the forces terms in S_x have been additionally classified, accordingly to equations (8), (15), (17), describing the three rheology models considered in this study. What follows is a summary of the force terms, and this notation will be used in the following (see Sections 4.2, 5.3).

Left-hand side, LHS forces

$$\mathbf{LHS}_1 = \left[\frac{\partial}{\partial t}(h\bar{u}), \frac{\partial}{\partial t}(h\bar{v}) \right], \quad (18)$$

it is the temporal derivative of momentum.

$$\mathbf{LHS}_2 = \left[\frac{\partial}{\partial x} \left(h\bar{u}^2 + \frac{1}{2}kg_z h^2 \right) + \frac{\partial}{\partial y}(h\bar{u}\bar{v}), \frac{\partial}{\partial x}(h\bar{u}\bar{v}) + \frac{\partial}{\partial y} \left(h\bar{v}^2 + \frac{1}{2}kg_z h^2 \right) \right], \quad (19)$$

it is the material derivative of momentum, due to the advection.

Right-hand side, RHS forces

$$\mathbf{RHS}_1 = [g_x h, g_y h], \quad (20)$$

it is the gravitational force term, it has the same formulation in all models.

The formula of basal friction force \mathbf{RHS}_2 depends on the model:

$$\begin{aligned} \mathbf{RHS}_2 &= -hg_z \tan(\phi_{bed}) \left[\frac{\bar{u}}{\|\tilde{\mathbf{u}}\|}, \frac{\bar{v}}{\|\tilde{\mathbf{u}}\|} \right], \text{ in MC model.} \\ \mathbf{RHS}_2 &= -hg_z \mu_b(\|\tilde{\mathbf{u}}\|, h) \left[\frac{\bar{u}}{\|\tilde{\mathbf{u}}\|}, \frac{\bar{v}}{\|\tilde{\mathbf{u}}\|} \right], \text{ in PF model.} \\ \mathbf{RHS}_2 &= -hg_z \mu \left[\frac{\bar{u}}{\|\tilde{\mathbf{u}}\|}, \frac{\bar{v}}{\|\tilde{\mathbf{u}}\|} \right], \text{ in VS model.} \end{aligned} \quad (21)$$

The formula of the force related to the topography curvature, \mathbf{RHS}_3 , also depends on the model:

$$\begin{aligned} \mathbf{RHS}_3 &= h \tan(\phi_{bed}) \left[-\frac{\bar{u}^3}{r_x \|\tilde{\mathbf{u}}\|}, -\frac{\bar{v}^3}{r_y \|\tilde{\mathbf{u}}\|} \right], \text{ in MC model.} \\ \mathbf{RHS}_3 &= h \mu_b(\|\tilde{\mathbf{u}}\|, h) \left[-\frac{\bar{u}^3}{r_x \|\tilde{\mathbf{u}}\|}, -\frac{\bar{v}^3}{r_y \|\tilde{\mathbf{u}}\|} \right], \text{ in PF model.} \\ \mathbf{RHS}_3 &= h \mu \left[-\frac{\bar{u} \|\tilde{\mathbf{u}}\|}{r_x} \mu, 0 \right], \text{ in VS model.} \end{aligned} \quad (22)$$

All the three models have an additional force term, having a different formula and meaning in the three models:

$$\begin{aligned} \mathbf{RHS}_4 &= -hk_{ap} \sin(\phi_{int}) \left[\operatorname{sgn} \left(\frac{\partial \bar{u}}{\partial y} \right) \frac{\partial(g_z h)}{\partial y}, \operatorname{sgn} \left(\frac{\partial \bar{v}}{\partial x} \right) \frac{\partial(g_z h)}{\partial x} \right], \text{ in MC model.} \\ \mathbf{RHS}_4 &= g_z h \left[\frac{\partial h}{\partial x}, \frac{\partial h}{\partial y} \right], \text{ in PF model.} \\ \mathbf{RHS}_4 &= -\frac{\|\mathbf{g}\|}{\xi} \|\tilde{\mathbf{u}}\|^2 \left[\frac{\bar{u}}{\|\tilde{\mathbf{u}}\|}, \frac{\bar{v}}{\|\tilde{\mathbf{u}}\|} \right], \text{ in VS model.} \end{aligned} \quad (23)$$

3.3 Definition and consistency of the input variables

In general, the three rheologies considered in this study, MC, PF, and VS, have totally different parameters. The statistical testing we perform requires to choose the parameter range P_M , and in principle it may be arbitrary. Nevertheless, if the total frictions of the models are not covering a similar span, the statistical comparison is dominated by trivial macroscopic differences, and cannot focus on the rheology details. Some degree of parameter consistency is required between the models.

We can find several instances of parameter choices in literature, and in general the choice depends on the case study. In all the models it is defined a basal friction stress (see RHS_2 in in 4). However, PF interpolates different effective friction angles, while VS includes a velocity based additional term. We tested that a direct correlation of effective friction angles is problematic to do. Hence, we did not follow such approach. In contrast, we make a preliminary testing on the extreme values of the parameter space, i.e. giving ***max volume – min resistance***, and ***min volume – max resistance***.

General definitions We assume what follows to simplify testing. Except when differently specified, parameters are sampled uniformly in linear scale.

- Material Volume V is an additional input parameter in all the models, on the same range.
- In MC, sampled input parameters are ϕ_{bed} , and $\Delta\phi := \phi_{int} - \phi_{bed}$. In particular, $\Delta\phi \in [2^\circ, 10^\circ]$ (?).
- In PF, sampled input parameters are ϕ_1 , $\Delta\phi_{12} := \phi_2 - \phi_1$, and β . In particular, $\Delta\phi_{12} \in [10^\circ, 15^\circ]$, and $\beta \in [0.1, 0.85]$. Moreover, $\phi_3 = \phi_1 + 1^\circ$, and \mathcal{L} is equal to 1 dm and 1 mm in the two case studies, respectively (????).
- In VS, sampled input parameters are μ , and ξ . In detail, ξ uniform sampling is accomplished in log-scale. In fact, values of ξ between 250 and 4,000 m/s^2 have been described for snow avalanches (???).

In summary, MC and VS have three-dimensional parameter spaces, while PF a four-dimensional parameter space.

Flow down an inclined plane In this case study, ? assumed $\phi_{bed} = [15^\circ, 30^\circ]$, while ? performed a series of laboratory experiments and found $\phi_{bed} = [18.2^\circ, 34.4^\circ]$. We relied on those published parameter choices to decide a comprehensive parameter range. Figure 4 displays the maps of max flow height and max velocities observed in the extreme cases tested. Simulation options are - `max_time = 2 s`, `height/radius = 1.34`, `length_scale = 1 m`, `number_of_cells_across_axis = 10`, `order = first`, `geoflow_tiny = 1e4` (??).

- **Material Volume:** $[449.0, 607.0] \text{ cm}^3$, i.e. average of 528.0 cm^3 and uncertainty of $\pm 15\%$.
- **Rheology models' parameter space:**

The parameter ranges adopted in this case study are:

$$\text{MC} - \phi_{bed} \in [18^\circ, 30^\circ].$$

$$\text{PF} - \phi_1 \in [10^\circ, 22^\circ].$$

$$\text{VS} - \mu \in [0.22, 0.45], \quad \log(\xi) \in [3, 4].$$

Even if maximum and minimum runout are both matching, the shape and lateral extent of the flow is remarkably different in the max. runout case, according to the three models. In particular, MC model can produce the largest lateral extent, and VS model displays an accentuated wedge-like shape, due to the increased friction in the lateral margins. These features will be detailed in Section 4.1.

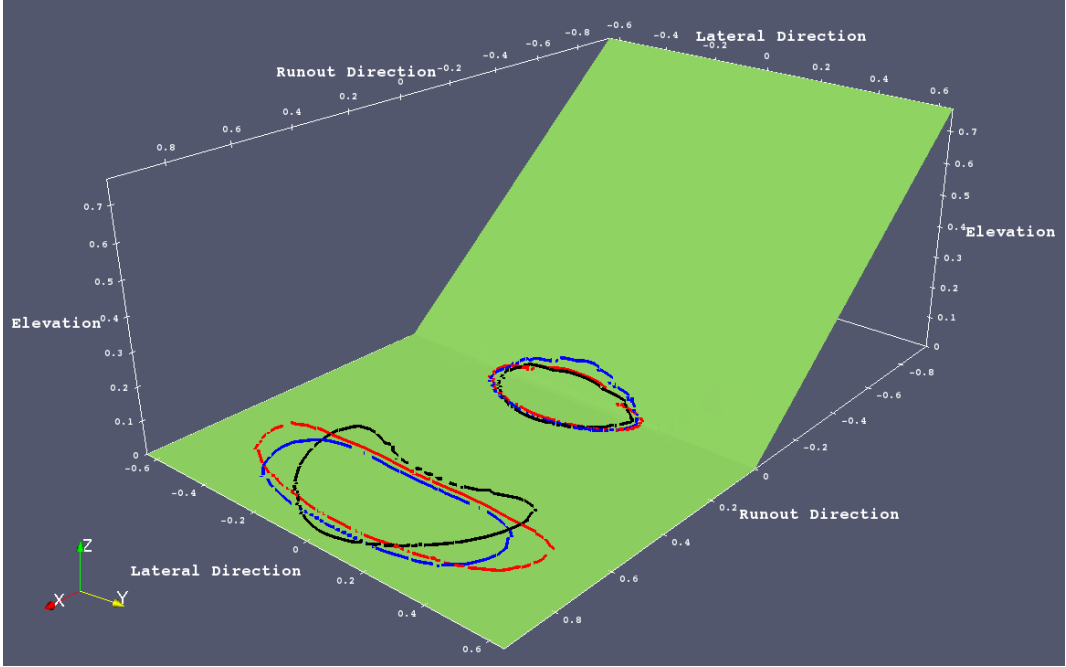


Figure 4: Inclined plane setup. Contours of $h = 1.0$ mm at last simulated snapshot ($t = 1.5$ sec) for simulated flows with *minimum runout* obtained from ***min volume – max resistance***, and *maximum runout* obtained from ***max volume – min resistance***. — : MC, — : PF, — : VS.

Volcán de Colima block and ash flow In this case study, ? assumed $\phi_{bed} = [15^\circ, 35^\circ]$, while (?) adopted $\phi_{bed} = 30^\circ$ in the simulation of a BAF in that same setting. Moreover, ??? found a statistical correlation between flow size and effective basal friction inferred from field observation of geophysical flows. The size of the BAF of this study would have $\phi_{bed} = [13^\circ, 18^\circ]$ according to their estimates. Figure 5 displays the maps of max flow height and max velocities observed in the extreme cases tested. Simulation options are - max_time = 7200 s (2 hours), height/radius = 0.55, length_scale = 4e3 m, number_of_cells_across_axis = 50, order = first, geoflow_tiny = 1e4 (??).

- **Material Volume:** $[2.08, 3.12] \times 10^5 \text{ m}^3$, i.e. average of $2.6 \times 10^5 \text{ m}^3$ and uncertainty of $\pm 20\%$.
- **Rheology models' parameter space:**

The parameter ranges adopted in this case study are:

$$\textbf{MC} - \phi_{bed} \in [10^\circ, 25^\circ].$$

$$\textbf{PF} - \phi_1 \in [8^\circ, 18^\circ].$$

$$\textbf{VS} - \mu \in [0.15, 0.45], \quad \log(\xi) \in [1.7, 4].$$

The models possess different features, even if the maximum runout after channelization in the ravines is matching. In particular, VS lateral spreading is significant lower and material reaches higher thickness, whereas PF model seems to stop more gradually than MC with a more complex inundated area boundary lines. These features will be detailed in Section 5.2.



Figure 5: Volcán de Colima BAF. Comparison between *max flow height* maps of simulated flow, assuming Mohr-Coulomb (a),(b), Pouliquen-Forterre (c),(d), and Voellmy-Salm (e),(f) rheology. Extreme cases producing maximum and minimum runout, i.e. (a),(c),(e) **max volume – min resistance** and (b),(d),(f) **min volume – max resistance**.

4 QoIs and Data Collected - Flow down and inclined plane, and a change in slope to a flat plane

First case study is the small scale experimental setting described above. First we describe the observable outputs (Section 4.1), and then the hidden dynamic quantities (Section 4.2). In many plots we note the effect of cutting the flow when height is < 1 mm, which is at the scale of the smallest granular size.

4.1 Observable outputs

Observable outputs include the flow height, speed, Fr , and acceleration as a function of time, measure on the four location L_1, \dots, L_4 displayed in Fig. 1. In addition, max lateral extension, flow area, and spatially averaged speed and Fr are displayed. UQ is also performed, accordingly to the parameter ranges described in Section 3.3.

4.1.1 Flow Height, local measurements

Figure 6 shows the flow height, $h(L, t)$, at the points $(L_i)_{i=1, \dots, 4}$, for the three rheology models.

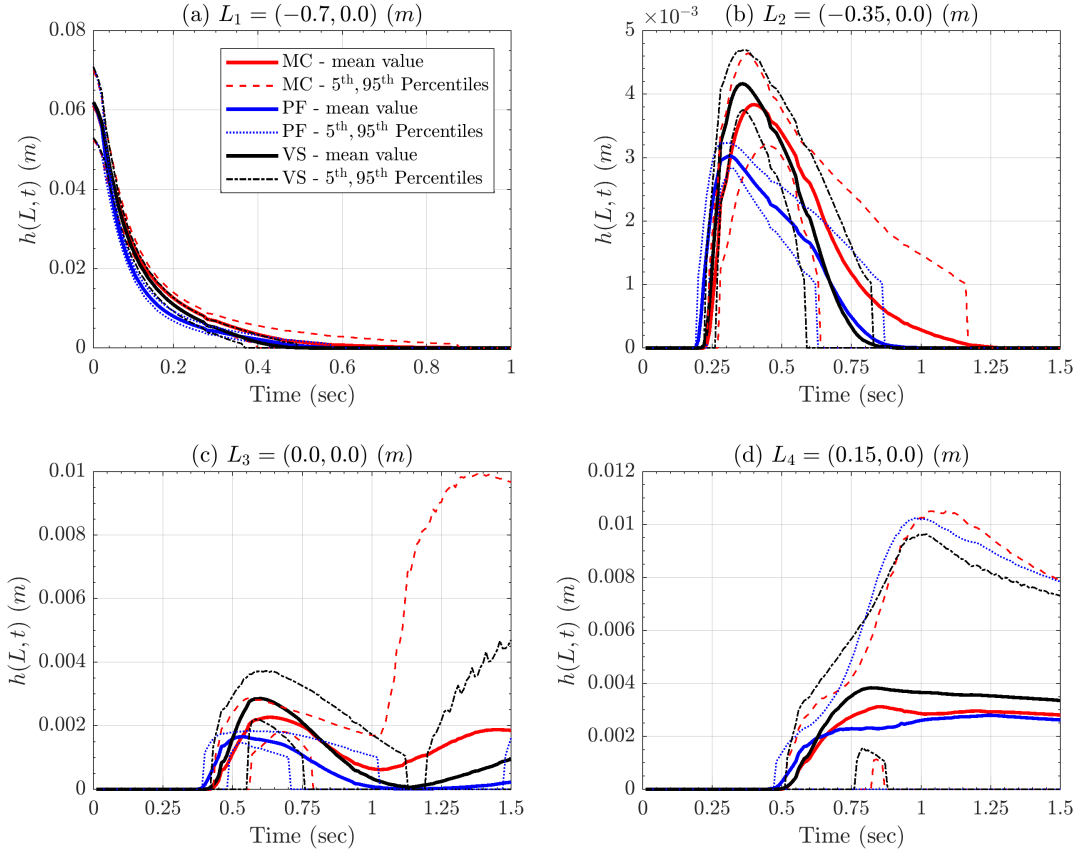


Figure 6: Records of flow height at four spatial locations of interest. Bold line is mean value, dashed/dotted lines are 5th and 95th percentile bounds. Different rheology models are displayed with different colors. Plots are at different scale, for simplifying lecture.

In plot (6a), related to point L_1 placed on the initial pile, the initial values of ~ 6 cm are the equal

and only represent the pile height uncertainty, but then the flow height decreases slightly faster for the PF model, and slower for the MC, compared to the VS. Difference are more significant in plot (6b), related to point L_2 , placed in the middle of the slope. Flow max height is greater for the VS, and smaller for the PF model, which decreases slower after the height peak. However, the value is ~ 15 times smaller than initial pile height, of ~ 4 mm. None of the models leaves a material deposit in L_1 or L_2 , i.e. the 95th percentile of the height is null at the ending-time. In contrast, a deposit is left at points L_3 , i.e. plot (6c) placed at the change in slope, and L_4 , i.e. plot (6d) in the middle of the flat runout. MC's deposit is higher than the other models' at L_3 , while it is not significantly different at L_4 between the three models. It is of ~ 3 mm in average, but can range from 0 to 8 mm. In plots (6b) and (6c) the elimination of material when height is < 1 mm, cuts the 95th percentile to zero when its value is below that threshold.

4.1.2 Flow Speed, local measurements

Figure 7 shows the flow speed, $\|\bar{\mathbf{u}}\|(L, t)$, at the points $(L_i)_{i=1,\dots,4}$, for the three rheology models.

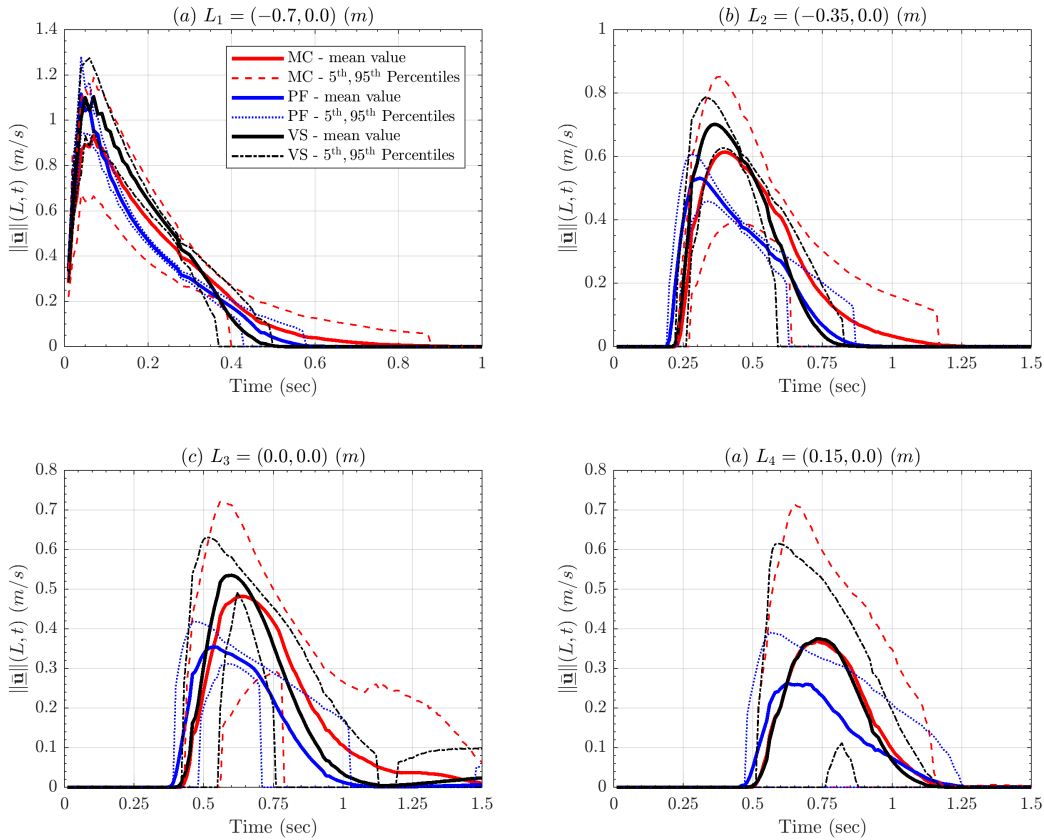


Figure 7: Records of flow speed at four spatial locations of interest. Bold line is mean value, dashed/dotted lines are 5th and 95th percentile bounds. Different rheology models are displayed with different colors. Plots are at different scale.

In plots (7a) and (7b), related to points L_1 and L_2 , speed peaks are similar between the models, at ~ 10 cm/s and ~ 6 cm/s, respectively. In plot (7a) VS peak is higher, but then its speed decreases more linearly, while MC and PF have a more concave profile, making MC the faster model after 0.5 sec. In plot

(7b) it is the PF model to decrease more linearly. UQ shows that MC model uncertainty is remarkably larger than in the other models, and produces higher values in the 95th percentile plots. Speed values below 1 cm/s are affected by the elimination of material below 1 mm flow height threshold. In plots (7c) and (7d), related to points L_3 and L_4 , the PF velocity profile is significantly lower than the other models, but it also decreases slower, and matches with the stopping times of them. Speed in the deposits is below 1 cm/s at L_3 , negligible at L_4 .

4.1.3 Froude Number, local measurements

Figure 8 shows the Froude Number, $\|\bar{\mathbf{u}}\|/\sqrt{gh}$, at the points $(L_i)_{i=1,\dots,4}$, for the three rheology models.

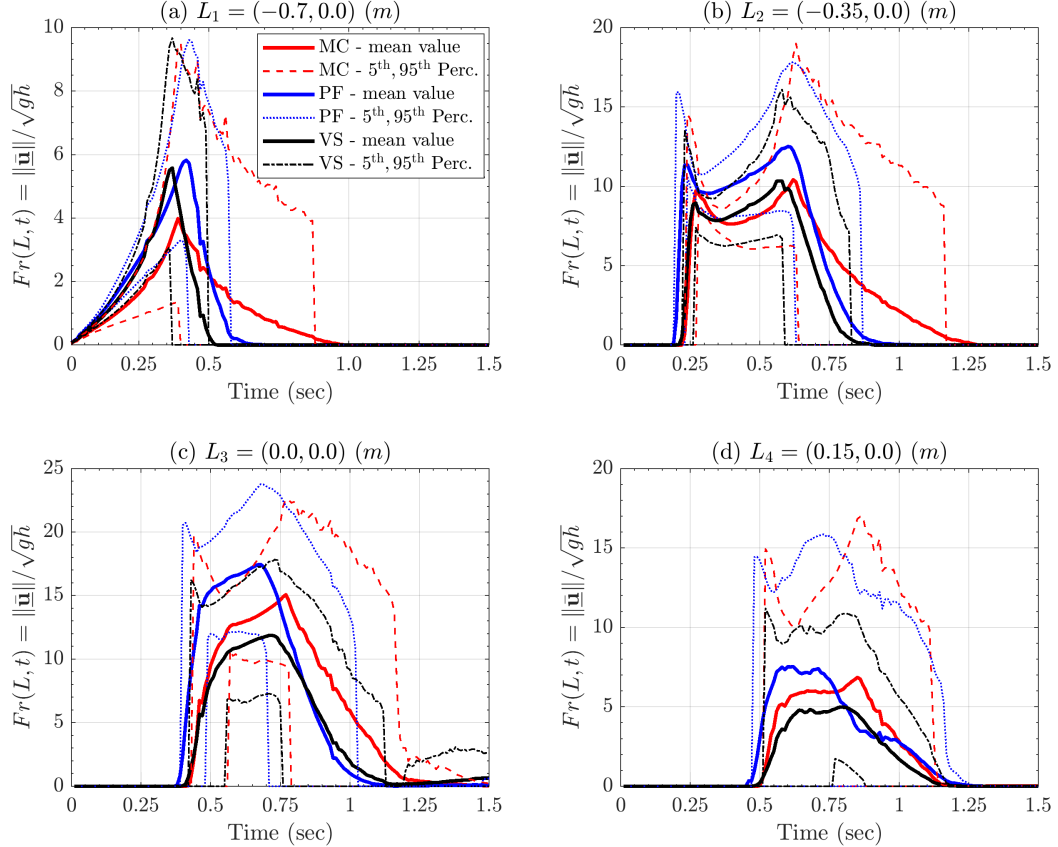


Figure 8: Records of Froude number at four spatial locations of interest. Bold line is mean value, dashed/dotted lines are 5th and 95th percentile bounds. Different rheology models are displayed with different colors. Plots are at different scale.

Froude Number combines the estimates of flow height and speed, described above. In plot (8a), related to point L_1 , Fr maximum average value is smaller for the MC model, ~ 4 , than for the others, ~ 6 . However, UQ tells us that 95th percentile almost reaches ~ 10 in all the three models. After the peak, the values decrease slower and more concavely in MC model than in the others. In plot (8b), related to point L_2 , Fr shows a bimodal profile in time, with two separate peaks at ~ 10 on average, but reaching ~ 18 in the 95th percentile plot. In fact, first maximum, at ~ 0.25 s is due to the speed peak, and second, at ~ 0.6 s is related to \sqrt{h} decreasing while the speed is not significantly changing. In plot (8c) and (8d), related to points L_3 and L_4 , bimodality is less accentuated and becomes a plateau profile

in $\sim [0.5, 0.75]$ sec. PF model gives significantly larger Fr values, even > 20 at L_3 , due to a larger speed and a thinner flow. It is worth noting, for the sake of PF model, that $Fr > \beta$ and the flow is in the dynamic regime during the most of the time.

4.1.4 Flow Acceleration, local measurements

Figure 9 shows the flow speed, $\|\bar{a}\|(L, t)$, at the points $(L_i)_{i=1,\dots,4}$, for the three rheology models.

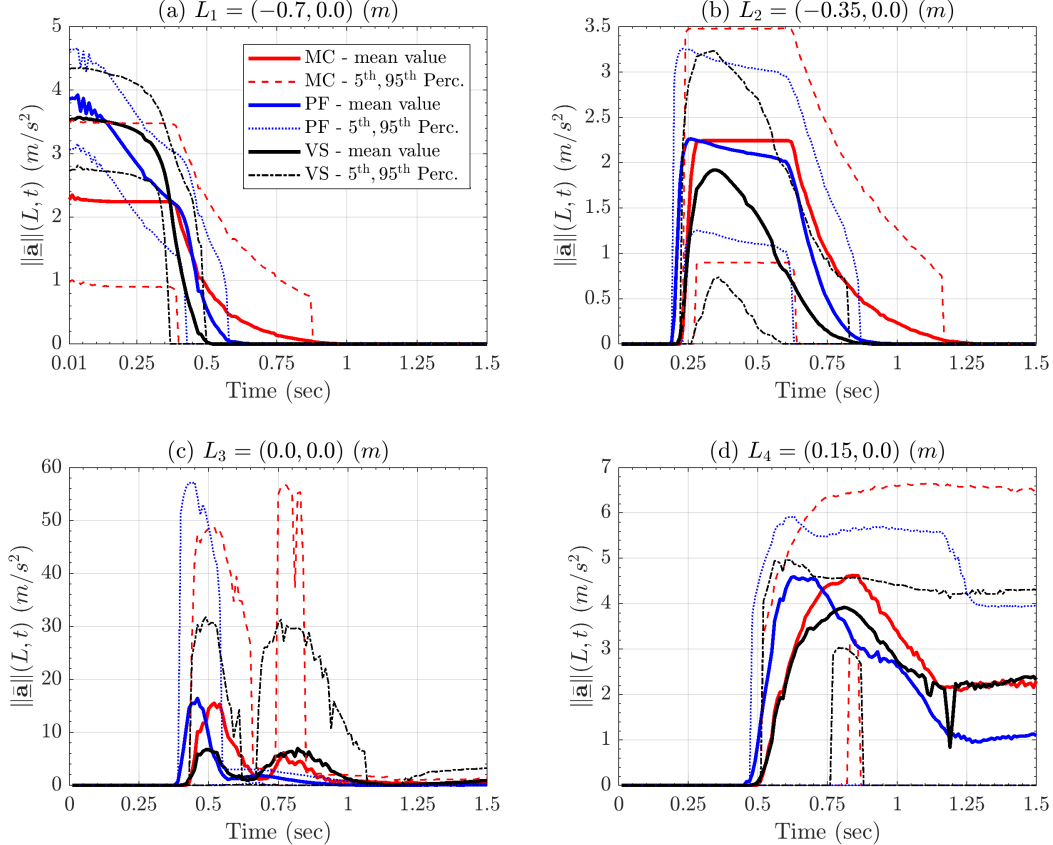


Figure 9: Records of flow acceleration magnitude (computed from LHS). Bold line is mean value, dashed lines are 5th and 95th percentile bounds. Different rheology models are displayed with different colors. Plots are at different scale.

Acceleration is the link between force terms and observable motion. We calculated it from the LHS of the dynamical equation, but using the RHS terms produces very similar results, although not identical due to the numerical approximations in our solution. In plot (9a), related to point L_1 , MC and VS show a plateau before ~ 0.4 sec, at $\sim 2.5 \text{ m/s}^2$ and $\sim 3.5 \text{ m/s}^2$, respectively, while PF linearly decreases between those same values. In plot (9b), related to point L_2 , are MC and PF to show a plateau, at $\sim 2.2 \text{ m/s}^2$, while VS has a more bell-shaped profile. UQ tells us that PF has a smaller uncertainty than the other models. In plot (9c), related to point L_3 , all the models show a bimodal profile, with peaks at ~ 0.5 sec and 0.8 sec. This is more accentuated for MC and VS, whereas the second peak is almost absent from PF profile. The second peak is motivated by an increase of velocity in the down-slope direction after its reduction due to lateral spreading of material. At the first peak, acceleration values are significant, with average peaks of MC and PF both at $\sim 15 \text{ m/s}^2$, and 95th percentile plot reaching

$\sim 50 \text{ m/s}^2$ and $\sim 55 \text{ m/s}^2$, respectively. VS shows about halved acceleration peak values. At the second peak, average acceleration values are similar for MC and VS, at $\sim 5 \text{ m/s}^2$. In contrast, 95th percentile plot is $> 50 \text{ m/s}^2$ for MC, while $\sim 30 \text{ m/s}^2$ for VS. In plot (9d), related to point L_4 , the acceleration has a first peak at $\sim 4 \text{ m/s}^2$, and a final asymptote at $\sim 2 \text{ m/s}^2$ for MC and VS, $\sim 1 \text{ m/s}^2$ for PF. These values generally mean flow deceleration, and uncertainty is more relevant for MC and PF than for VS.

4.1.5 Flow extents and averaged measurements

Figure 10 shows the spatial average of speed and Froude Number, for the three rheology models. Moreover, it shows the (maximum) lateral extent and inundated area of flow, as a function of time.

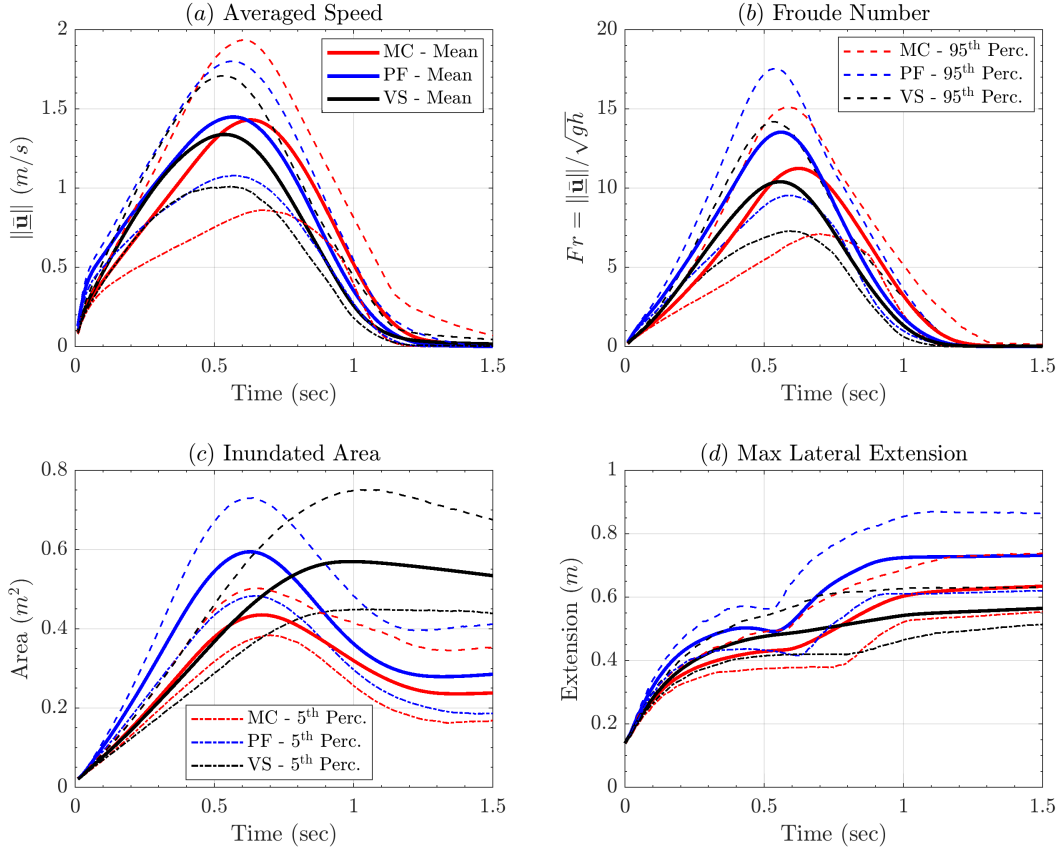


Figure 10: Comparison between spatial averages of (a) flow speed, and (b) Froude Number in addition to the flow (c) lateral extent, and (d) inundated area, as a function of time.

Spatial averages and global quantities as maximum lateral extent and inundated area have smoother plots than local measurements. Most of the details observed in local measurements are not easy to discern. In plot (10a) the speed show a bell-shaped profile in all the models, with an average peak at $\sim 1.4 \text{ m/s}$ and uncertainty range, given by 5th and 95th percentiles, of $\pm 0.4 \text{ m/s}$ for PF and VS. VS is slightly slower, reaching $\sim 1.3 \text{ m/s}$ in the average. MC shows a larger uncertainty range, of $\pm 0.6 \text{ m/s}$. The maximum speed is reached first by VS and PF at $\sim 0.55 \text{ s}$, and last by MC at $\sim 0.65 \text{ s}$. In plot (10b), also Froude Numbers have a bell-shaped profile. Fr peaks are temporally aligned with speed peaks, and are ~ 10 in VS, ~ 11 in MC, ~ 13.5 in PF, on average. Uncertainty range is about ± 4 in all models. In plot (10c) inundated area shows similar max values in PF and VS, at $\sim 0.6 \text{ m}^2$ on average, and uncertainty

of $\pm 0.15m^2$. MC is lower, at $\sim 0.45m^2$ on average, and less uncertain, $\pm 0.10m^2$. VS does not decrease significantly after reaching the peak, whereas the other models contract their area, to approximately half of the maximum extent. In plot (10d) the lateral extent starts equal to the pile diameter 15cm, and then rises in two stages in MC and PF, the second and greater rise starting at $\sim 0.6s$, corresponding to the time of arrival at the change in slope L_3 (see Fig. 6c). VS rises without showing two phases. After the first phase, average lateral extent is at $\sim 50cm$ in PF and VS, while it is $\sim 43cm$ in MC. Uncertainty range is $\pm 7cm$ for all models at that time. Final extent is $\sim 75cm$ in PF, $\sim 65cm$ in MC, $\sim 55cm$ in VS. Uncertainty range is $\pm 5cm$ in VS, but rises to $\pm 10cm$ in MC and PF.

4.2 Hidden dynamic quantities

These include force terms and related powers, as well as their statistical analysis. The classification follows the definitions in section 3.2.

4.2.1 Forces, spatial average

Figure 11 shows the spatial average of force terms in the slope direction, for the three rheology models. In plot (11a) \mathbf{RHS}_1 represents the effect of the gravity in all the models. It starts with a plateau at $\sim 1.3N$ before $\sim 0.55s$, then decreases to zero after the material crosses the change in slope. Uncertainty range of $\pm 0.2N$ on the peak values. MC decreases slower, and has a more significant uncertainty, after the change in slope. PF decreases faster. In plot (11b) \mathbf{RHS}_2 represent the friction at the base of the flow. It is negative and opposed to the gravity. A similar profile is shared by the three models, with a first short-lasting weakening before $\sim 0.1s$, a plateau with a small strengthening after $\sim 0.5s$, and a final waning after $\sim 1s$, at the conclusion of the dynamics. MC does not reach zero, while the other models do. VS values are generally $\sim 0.5N$ weaker than MC, and PF is intermediate, except in the initial peak, where it is the weakest. Strongest forces are reached during the plateau, and are $\sim -0.55N$, $\sim -0.75N$, $\sim -0.9N$, with uncertainty range of $\pm 0.25N$ in the plateau. Uncertainty is reduced in the final stages of VS and PF, but increases in MC. In plot (11c) \mathbf{RHS}_3 is related to the curvature effects, and is not null only at the change in slope. It is always negative, i.e. reducing flow velocity, indeed it is equivalent to the friction due to the additional weight generated by centrifugal forces. Its scale is ten times smaller than the previous plots, with values above $0.1N$ only in MC. VS displays a bimodal profile, with a second and weaker peak at $\sim 0.75s$. In plot (11d) \mathbf{RHS}_4 is related to the additional forces of the models, differently characterized. In MC and PF, they are significantly small forces before $0.1s$, completely negligible later. In VS, this is the velocity dependent term. It is negative and plays a significant role. It reaches $\sim 1N$ at the change in slope, with uncertainty $\pm 0.3N$. It is bell shaped and null before $\sim 0.1s$ and after $\sim 1s$. In plot (11e) $\sum_{i=1}^4 \mathbf{RHS}_i$ represents the total force in the slope direction, and summarizes the previous plots. The profile is characterized by a positively valued stage at $\sim 0.5N$ before the change in slope, and by a negatively valued stage after that, with bell-shaped profile, and a peak at $\sim -0.5N$. In the first stage MC is more flat, while PF and VS decrease. In the second stage MC is occurring later in time, of $\sim 0.1s$; PF and VS are remarkably similar, but VS wanes faster.

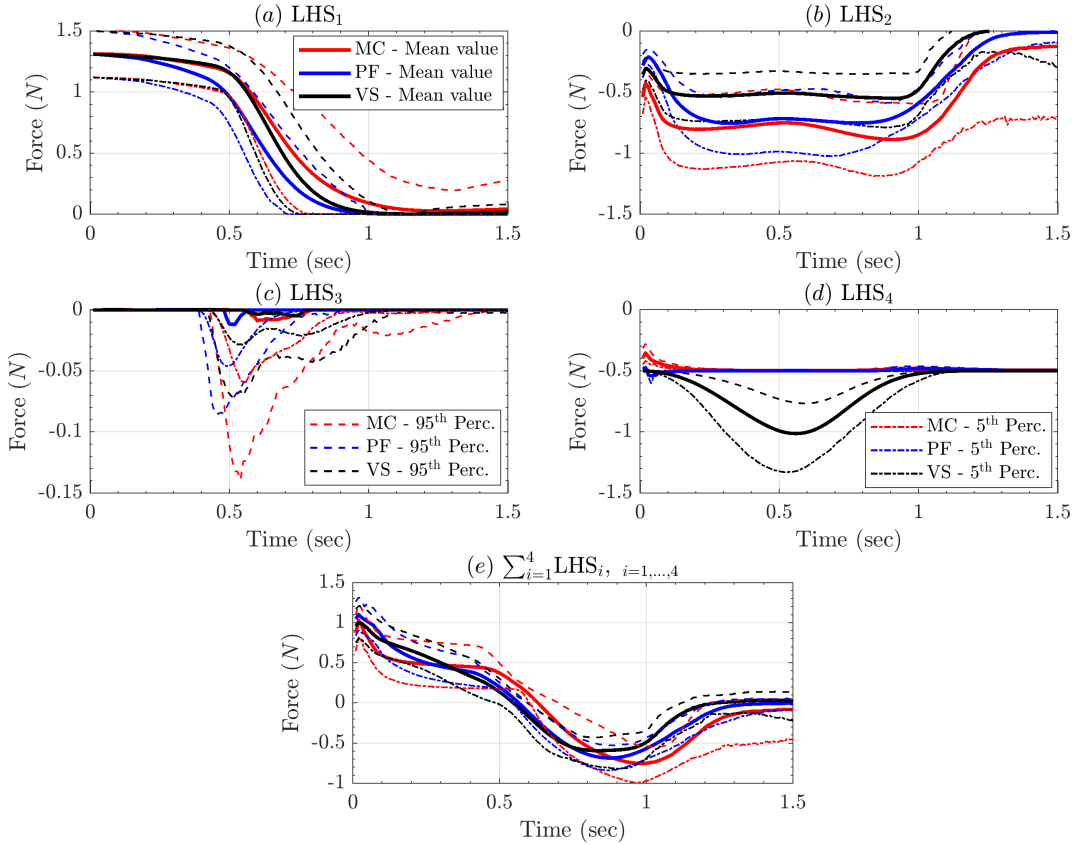


Figure 11: Spatial average of the RHS forces in the slope direction. Bold line is mean value, dashed lines are 5th and 95th percentile bounds. Scale of plot (c) is ten times larger than in (a),(b),(d); scale of plot (e) is slightly smaller.

4.2.2 Powers, spatial average

Figure 12 shows the spatial average of powers, for the three rheology models. The plots follow the same order used in Fig. 11, but the scalar product with velocity imposes the bell-shaped profile observed in Fig. 10a. In plot (12a) the power of \mathbf{RHS}_1 starts from zero and rises up to $\sim 1.5J$, with uncertainty of $\pm 0.5J$. In plot (12b) the power of \mathbf{RHS}_2 is negative and peaks to $\sim 1J$ in MC and PF, $\sim 0.7J$ in VS. The initial ripple observed in Fig. 11b is not observed, nor the plateau. In plot (12c) the power of \mathbf{RHS}_3 has a similar profile to the force it is weaker than $-0.1J$ on average, although MC uncertainty reaches $\sim -0.25J$. In plot (12d) the power of \mathbf{RHS}_4 is relevant only in VS, although also in PF has a very short lasting positive peak up to $0.3J$ before to become null at $\sim 0.1s$. Power in VS is $\sim -0.7J$, $\pm 0.3J$. In plot (12e) the power of the total force $\sum_{i=1}^4 \mathbf{RHS}_i$ summarizes the energy accumulation and dissipation, following a sinusoid profile. As observed in Fig. 11e, MC profile is delayed of $\sim 0.1s$ compared to the others, and is affected by a larger uncertainty.

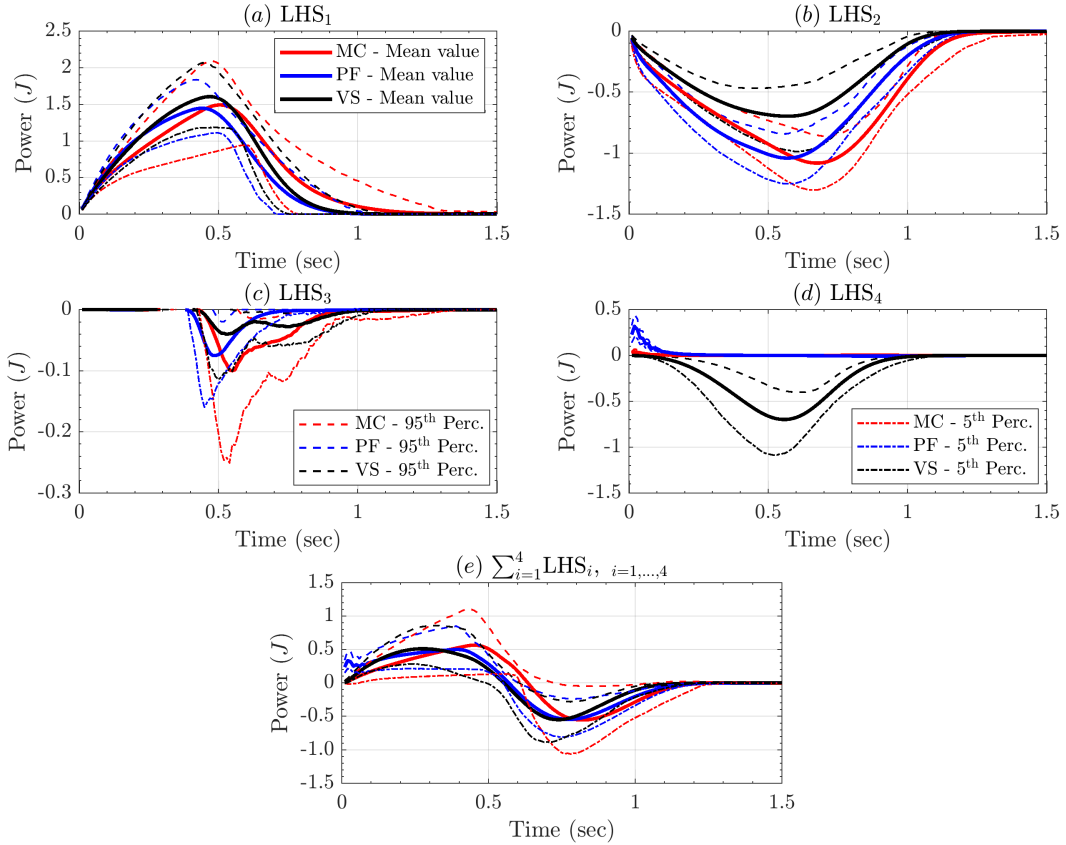


Figure 12: Spatial average of the RHS powers. Bold line is mean value, dashed lines are 5th and 95th percentile bounds. Model comparison on the mean value is also displayed.

4.2.3 Force contribution coefficients, RHS terms

Figure 13 shows the Contributions Coefficients (C_i) $_{i=1,\dots,4}$, for the three rheology models and focusing on the RHS terms in the slope direction. Force contributions are defined in section 3.1 and are obtained dividing the force terms described in section 3.2 by a dominant function Φ and taking the average. It is a tool to compare the different force terms, scaling the plots by the dominant function Φ - in this case in $[-1, 1]$. It also represent the degree of relevance of the assumptions behind the force terms, changing as a function of time. The different models are plotted separately: (13a,d,g,j) assume MC; (13b,e,h,k) assume PF; (13c,f,i,l) assume VS.

The plots (13a,b,c) are related to point L_1 , placed on the initial pile. C_1 and C_2 play the major roles, with a minor contribution C_4 in VS. Contributions profiles are flat plateaus that start to wane after 0.4s, with the rise of the probability of no-flow at the point L_1 (see also Fig. 14). Uncertainty is related to the no-flow times, and to the value of C_2 . The negative contribution C_4 can be significant, as it is shown by the 5th percentile values, but appears after 0.25s. The plots (13d,e,f) are related to point L_2 , placed in the middle of the slope. Again the major contributions are C_1 and C_2 , with trapezoidal profile preceded and followed by no-flow. In VS, C_4 becomes as a significant as C_2 , but it is bimodal instead than trapezoidal. The plots (13g,h,i) are related to point L_3 , placed at the change in slope. The contributions C_1 and C_2 are still the largest, but their profiles are bell-shaped. In VS, C_4 is almost identical to C_2 . In all the models, C_3 is also significant, with a peak similar to C_2 , but has a different profiles - triangular for MC and PF, bimodal for VS. In MC the decrease occurs in two stages. The

uncertainty tells us that C_3 can also be the dominant force, for a shorter time. Due to the presence of deposit, all the contributions are small (particularly small in PF), but not zero at the ending time. The plots (13j,k,l) are related to point L_4 , placed in the middle of the flat runout. Only C_2 has a major role, with a bell shaped profile faster to wax than to wane. Contribution C_4 has a minor role in VS and PF. Uncertainty affects this force, which can be shortly the dominant term, in PF.

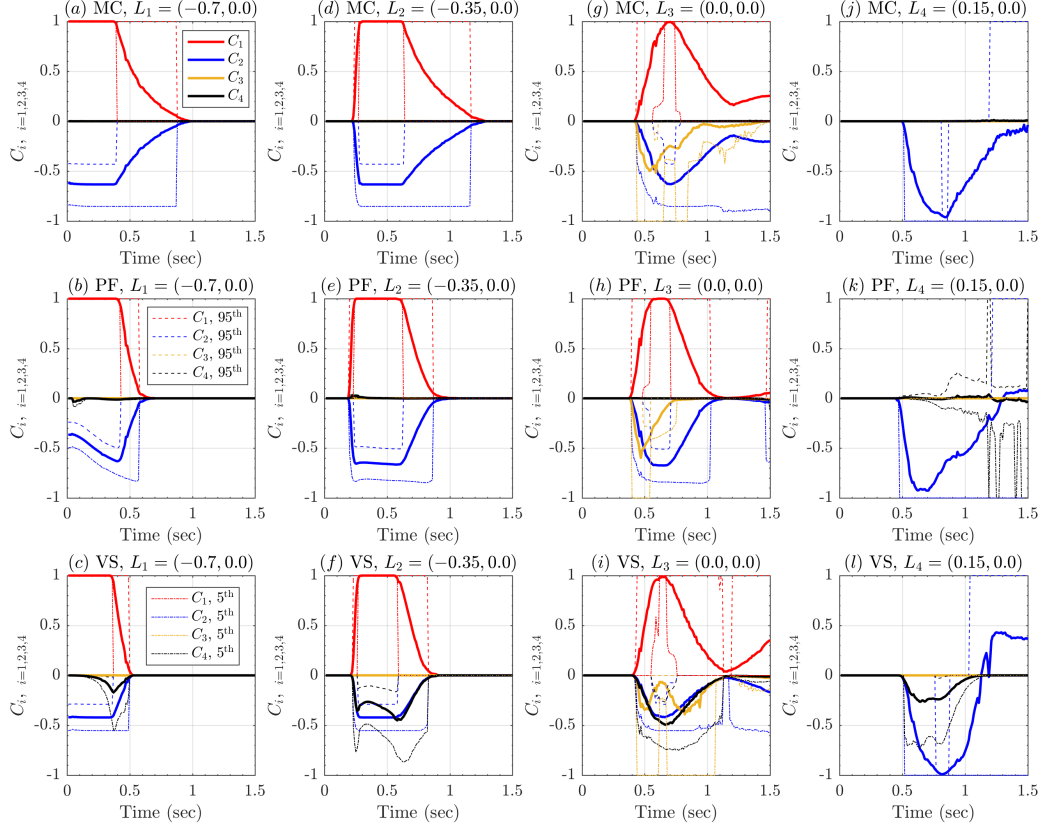


Figure 13: Records of contribution coefficients of **RHS** forces, in the slope direction, in four spatial locations of interest. Bold line is mean value, i.e. the Contribution Coefficient, while dashed/dotted lines are 5th and 95th percentile bounds associated to it. Different rheology models are displayed with different colors. Dominant function Φ is calculated based on the l^∞ norm (see Section 3.1)

4.2.4 Force dominance factors, RHS terms

Figure 14 shows the Dominance Factors $(P_i)_{i=1,\dots,4}$, for the three rheology models and focusing on the RHS terms in the slope direction. They are defined in section 3.1 and are the probability of each force term (described in section 3.2) to be the maximal one. It is another tool to compare the different force terms, following a more strict approach than the Contribution Coefficients. The values are probability values, hence in $[0, 1]$. The plots include also the probability of no-flow in the considered point. Similarly to Fig. 13, the different models are plotted separately: (14a,d,g,j) assume MC; (14b,e,h,k) assume PF; (14c,f,i,l) assume VS.

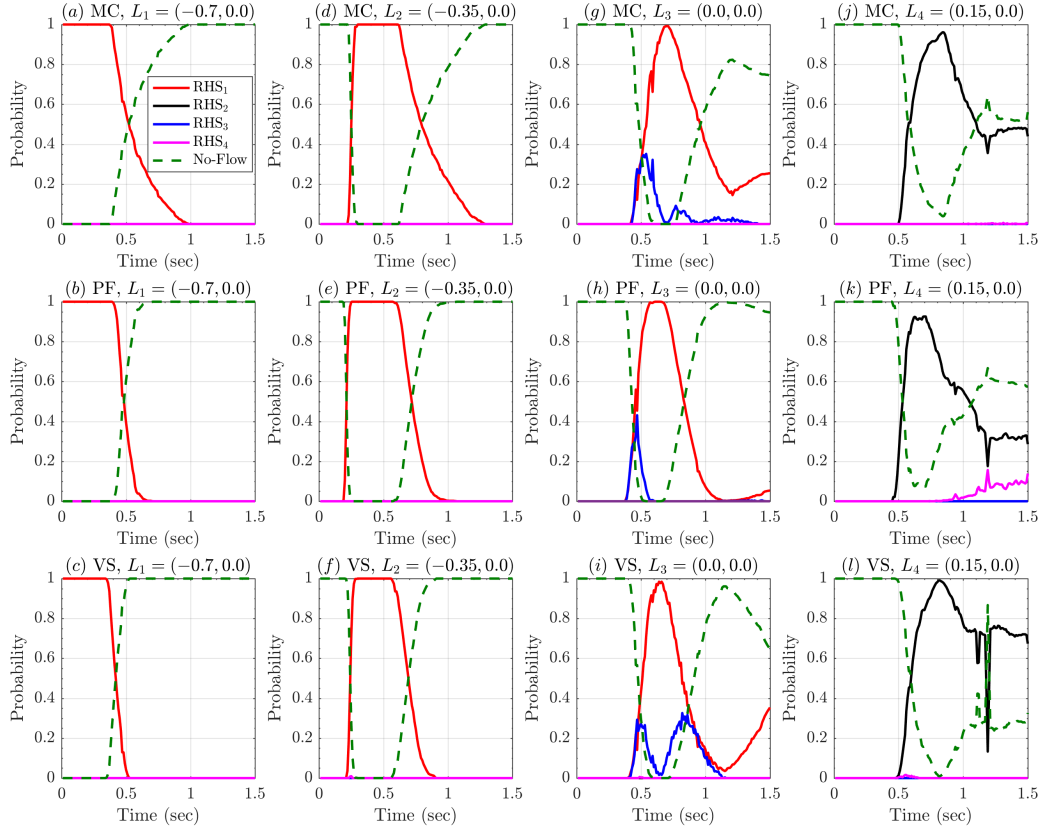


Figure 14: Records of dominance probabilities of **RHS** forces, in the slope direction, in four spatial locations of interest. Different rheology models are displayed with different colors. No-flow probability is also displayed with a green dashed line.

The plots (14a,b,c) are related to point L_1 , placed on the initial pile. Only **RHS₁** can be the dominant force, and no-flow probability is $(1 - P_1)$. Same thing in the plots (14d,e,f) are related to point L_2 , placed in the middle of the slope. The plots (14g,h,i) are related to point L_3 , placed at the change in slope. As observed in Fig. 13, also **RHS₃** can be the dominant term for a short time, with a peak probability of $\sim 30\%$. The plots (14j,k,l) are related to point L_4 , placed in the middle of the flat runout. Only **RHS₂** can be the dominant term, except in PF where there is $\sim 10\%$ that **RHS₄** is the dominant term at then ending-time.

5 QoIs and Data Collected - Volcán de Colima BAF

5.1 Observable outputs overview - MC model

In our second case study, the number of spatial locations is significantly higher than previously. In fact, we placed 51 points to span the entire inundated area, in search of different flow regimes, displayed in Fig. 2. First we show the average flow height, speed, and Fr in all the locations, then, based on that, we select six points which we find representative of interesting flow regimes. Figures 15, 16, 17 assume MC model, while the results related to PF and VS models are included in the Supporting Material.

5.1.1 Average flow Height, local measurements.

Figure 15 shows the flow height, $h(L, t)$, at the 51 spatial locations of interest, according to MC.

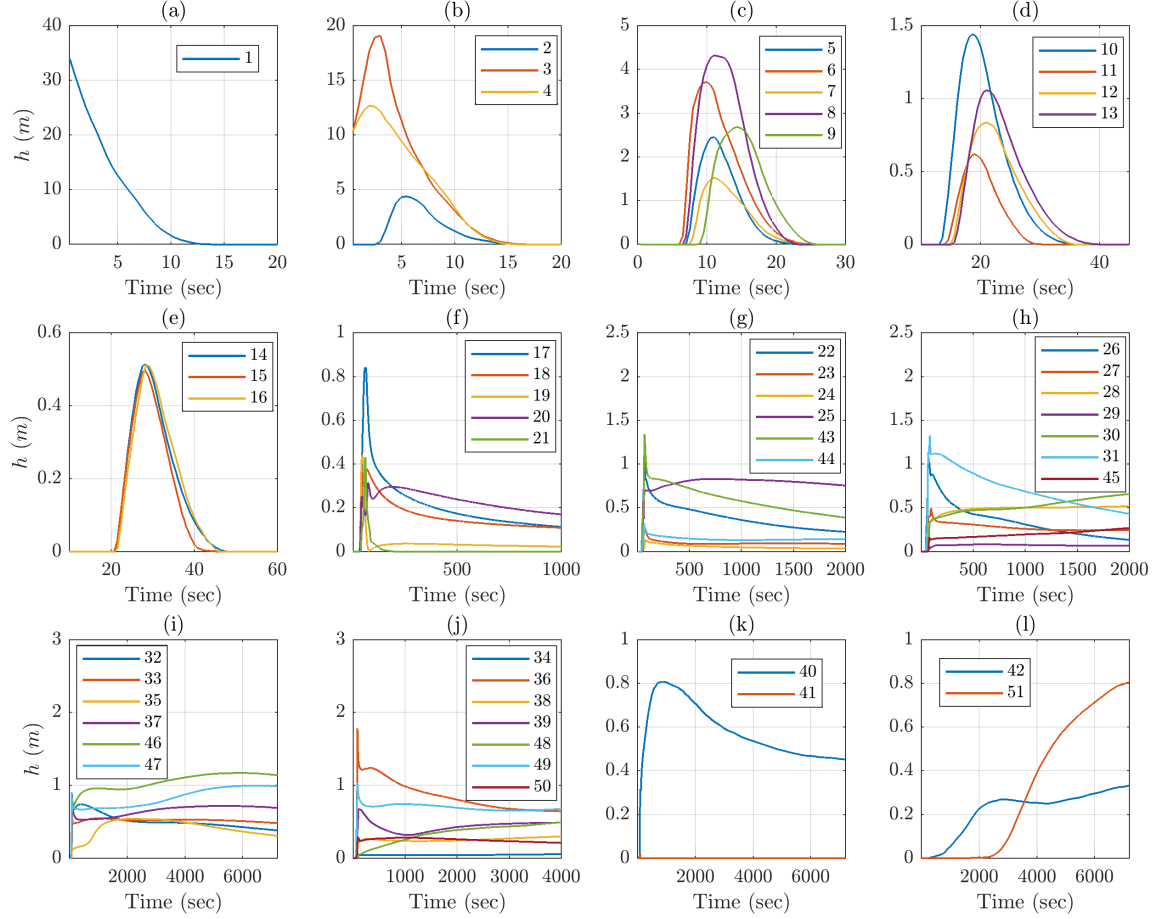


Figure 15: MC model, records of average flow height, $h(L, t)$, in 51 spatial locations of interest (Fig. 2).

Different plots have different scales on either time and space axes. In plot 15a, the only location is set on the center of the initial pile, and the profile is similar to what observed in point L_1 of the inclined plane case study, in Fig.6a. In particular, the height decreases from the initial value to zero, in about 15 s. In plots 15b,c,d,e, the locations are set at less than ~ 1 km radius from the initial pile (projected distance, without considering slope). Their profiles are similar to point L_2 in Fig.6b. The height profile is bell-shaped, starting from zero and then waning back to zero in ~ 20 s. All the dynamics occurs during the first minute. Plot (b) shows transitional features, and focuses on points at the boundary of the initial pile. In plots 15f,g,h,i,j, points are set where the slope reduces, and the flow can channelize and leave a deposit. Projected distance from the initial pile is $\sim 2 - 3$ km. The profiles are sometimes similar to L_3 of Fig.6c, other times to L_4 of Fig.6d, in a few cases showing intermediate aspects. In general is either observed an initial short-lasting bulge followed by a slow decrease lasting minutes and asymptotically tending to a positive height, or a steady increase of material height tending to a positive height. In both cases it is sometimes observed a bimodal profile in the first 5 minutes. Finally, plots 15k,l focus on three points set at about the runout distance of the flow, in the most important ravines,

at $\sim 4 - 5$ km projected distance from the initial pile. Profiles are similar to what observed in point L_4 of Fig.6d.

5.1.2 Average flow Speed, local measurements.

Figure 16 shows the flow speed, $h(L, t)$, at the 51 spatial locations of interest, according to MC.

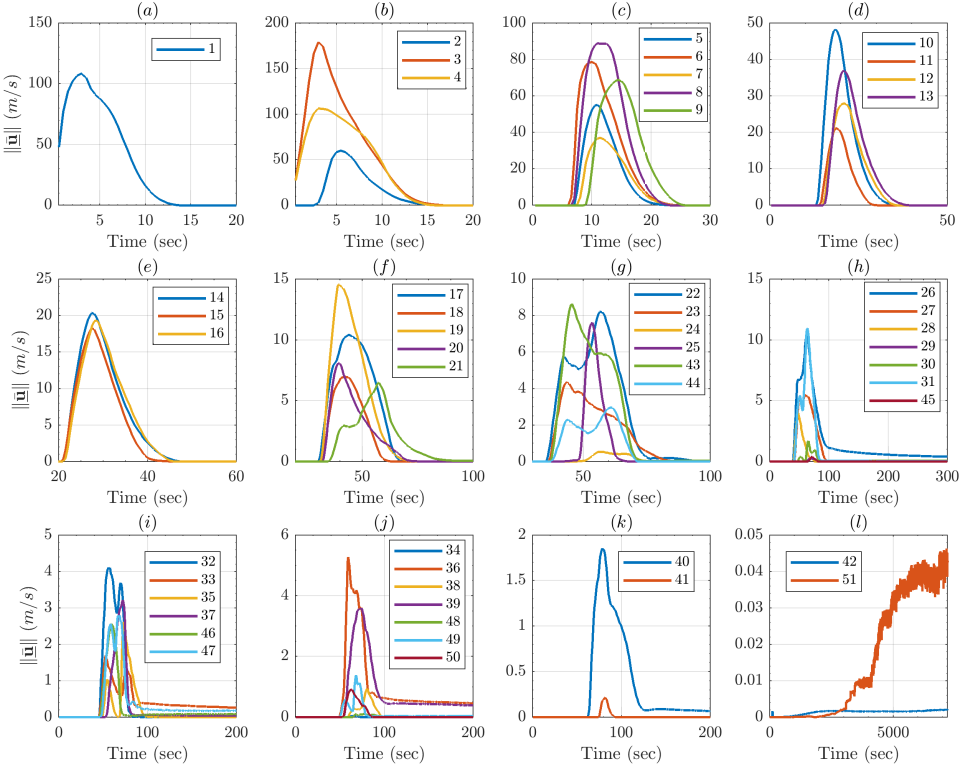


Figure 16: MC model, records of average flow speed, $|\underline{u}|(L, t)$, in 51 spatial locations of interest (Fig. 2).

Again the different plots have different scales on either time and space axes. The plot profiles are similar to what observed in figure 7, following the plot profile classification described above. In detail, in plots 16f,g,h,i,j, the speed often shows bimodal profiles, not observed in the inclined plane case study. Moreover, in plots 16h,i,j, positive asymptotes are sometimes observed, meaning a slowly and steadily moving material even minutes after the collapse.

5.1.3 Average Froude Number, local measurements.

Figure 17 shows the Froude Number, $\|\underline{u}\|/\sqrt{gh}$, at the 51 spatial locations of interest, according to MC.

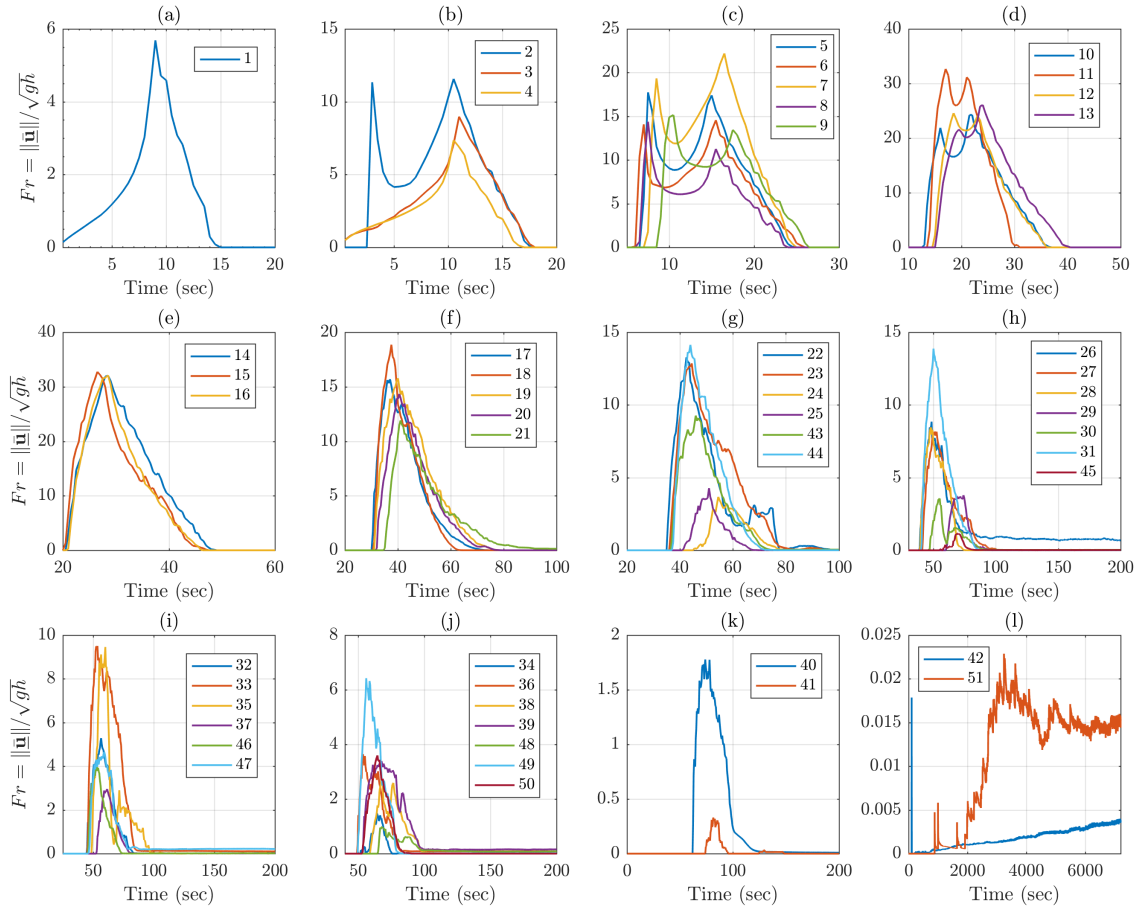


Figure 17: MC model, records of average Froude Number in 51 spatial locations of interest (Fig. 2).

Froude Number combines height and speed measurements, and plot profiles are similar to what observed in Figure 8. In particular, in plots 17b,c,d, strongly bimodal profile are observed. In plots 17f,g,h,i,j, sharp changes are observed, and the plots are significantly rough.

5.2 Observable outputs - six selected locations

The six selected locations are $[L_8, L_{10}, L_{17}, L_{39}, L_{43}, L_{46}]$, (see Fig. 2). First two points, L_8 and L_{10} are both significantly close to the initiation pile, the points L_{17} and L_{43} are placed where the slope is reducing and the ravine channels start, and L_{39} and L_{46} are placed in the channels, further down-slope. Moreover, L_8 , L_{43} , and L_{46} are placed at the western side of the inundated area, whereas L_{10} , L_{17} , and L_{39} are placed at the eastern side.

5.2.1 Flow Height, selected measurements

Figure 18 shows the flow height, $h(L, t)$, at the points $(L_i)_{i=8,10,17,39,43,46}$, for the three rheology models.

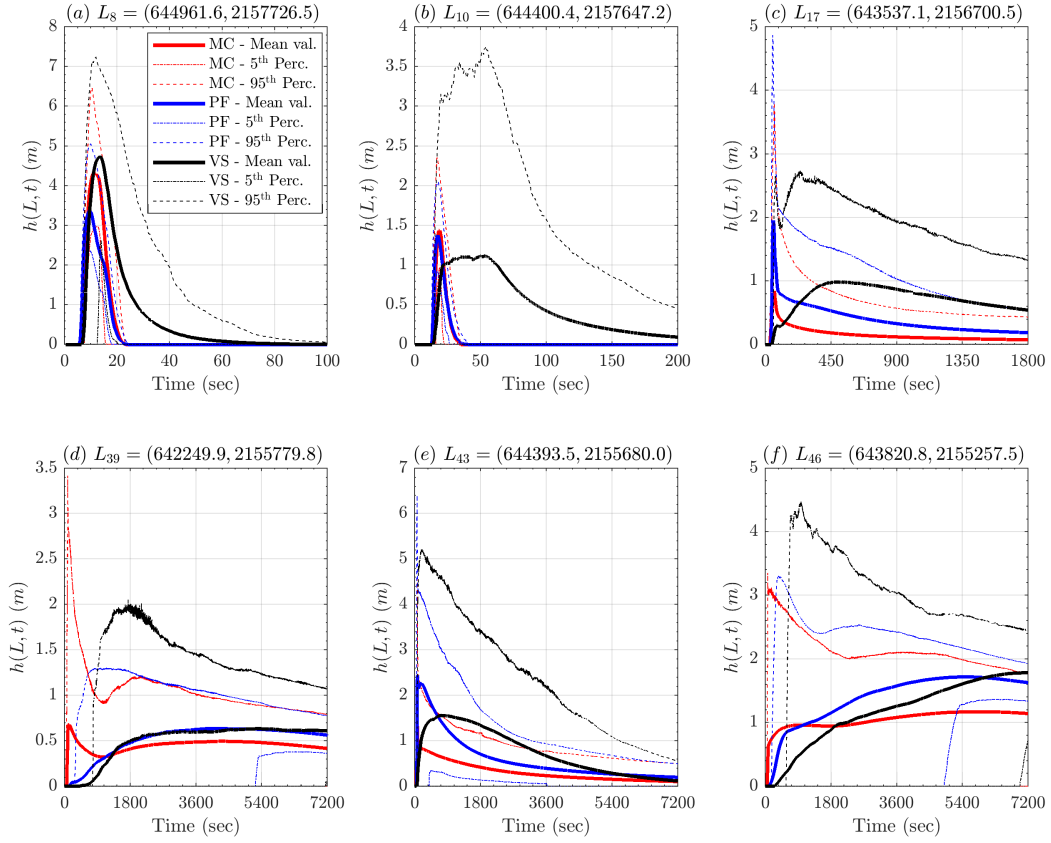


Figure 18: Records of flow height at six selected locations. Bold line is mean value, dashed/dotted lines are 5th and 95th percentile bounds. Different rheology models are displayed with different colors. Plots are at different scale, for simplifying lecture.

In plots 18a,b, we show the flow height in points L_8 and L_{10} , $\sim 200m$ and $\sim 500m$ from the initial pile, respectively. L_8 is on the east side, and L_{10} on the west side of the flow. Models MC and PF have similar profiles, lasting less $\sim 15s$ and bell-shaped. VS requires a significantly longer time to decrease, particularly in point L_{10} , where the average flow height is still positive after $\sim 200s$. Peak average values in L_8 are 3.4m for PF, 4.3m for MC, 4.7m for VS, with uncertainty of $\sim \pm 2m$, halved on the lower side for MC, and PF. In L_{10} , models MC and PF are almost indistinguishable, with peak height at 1.4m and uncertainty $\pm 0.5m$. Model VS, in contrast, has a maximum height of 1.1m lasting for 50s, and 95th percentile reaching 3.7m. In plots 18c,e, we show the flow height in points L_{17} and L_{43} , both at $\sim 2km$ from the initial pile, on the west and east side of the flow, respectively. All the three models show in both the points a fast spike in the first minute, followed by a slow decrease, still showing a positive average height after 30 m. Again, VS is significantly different from MC and PF, and has a secondary rise peaking at $\sim 450s$, which is not observed in the other models. This produces higher values for the most of the temporal duration, but converges to similar deposit thickness after more than 1 hour. Maximum values are 1m for MC, 2m for PF, and 1.5m for VS, in both locations. The 5th percentile is zero for all the three models, meaning that the parameter range does not always allow the flow to reach those locations. The 95th percentile is above 5m for the models, except in VS, point L_{17} . In plots 18d,f, we show the flow height in points L_{39} and L_{46} , both at more than 3km from the initial pile, on the west and east side of the flow, respectively. The three models all show an increasing profile, except for MC in point L_{39} which has an initial spike and a decrease before to rise again. A similar decreasing profile can be also observed

in the 95th percentiles of all the models. It is significant that the 5th percentile of PF becomes positive after $\sim 5400s$, meaning that the flows almost surely have reached that location. Deposit thickness is $\sim 0.5m$ for all the models in point L_{39} , and $1.7m$ for VS, $1.6m$ for PF, $1.2m$ for MC, in L_{46} .

5.2.2 Flow Speed, selected measurements

Figure 19 shows the flow speed, $\|\underline{\mathbf{u}}\|(L, t)$, at the points $(L_i)_{i=8,10,17,39,43,46}$, for the three rheology models.

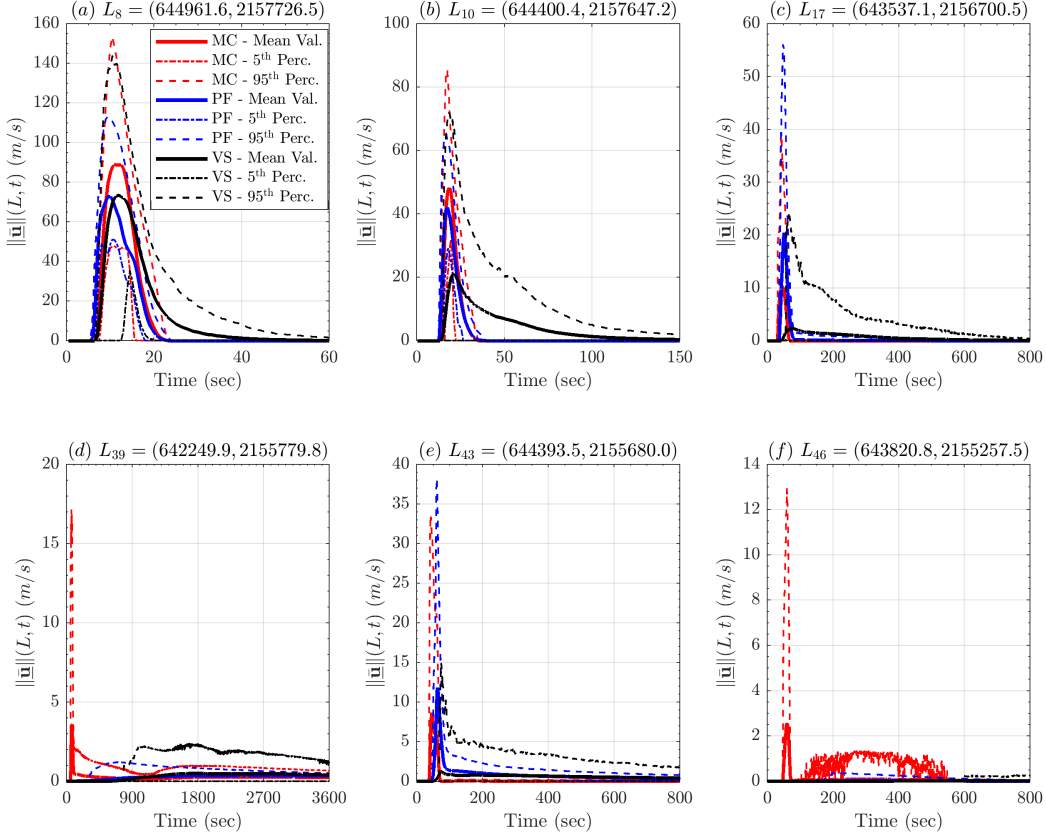


Figure 19: Records of flow speed at six selected locations. Bold line is mean value, dashed/dotted lines are 5th and 95th percentile bounds. Different rheology models are displayed with different colors. Plots are at different scale.

5.2.3 Froude Number, selected measurements

Figure 20 shows the Froude Number, $\|\underline{\mathbf{u}}\|/\sqrt{gh}$, at the points $(L_i)_{i=8,10,17,39,43,46}$, for the three rheology models.

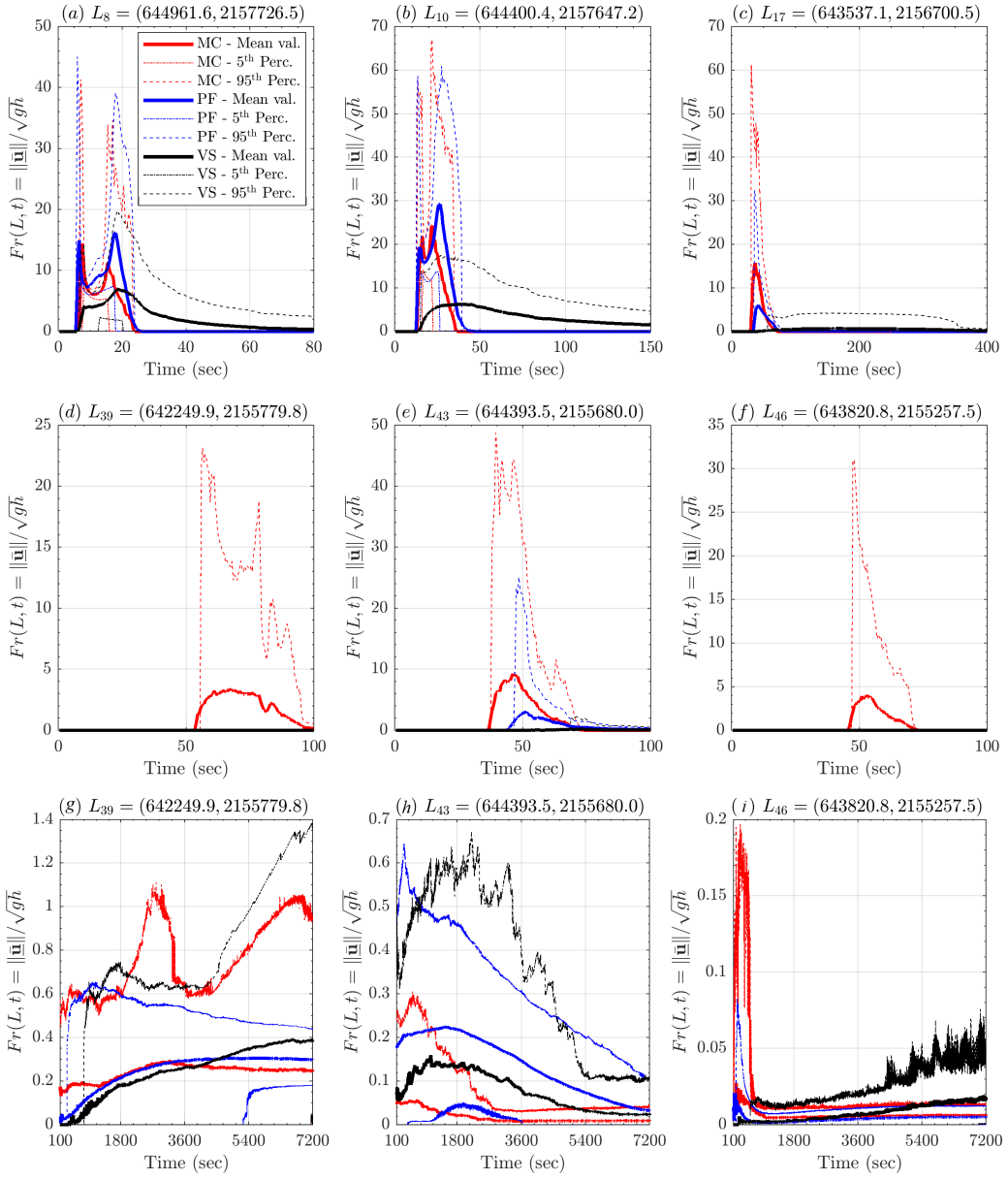


Figure 20: Records of Froude number at six selected locations. Records of points L_{39} , L_{43} , and L_{46} are displayed at two different scales, according to the initial dynamics, in plots (d-f), and the asymptotic dynamics, in plots (g-i). Bold line is mean value, dashed/dotted lines are 5th and 95th percentile bounds. Different rheology models are displayed with different colors.

5.2.4 Flow Acceleration, selected measurements

Figure 21 shows the flow speed, $\|\underline{\mathbf{a}}\|(L, t)$, at the points $(L_i)_{i=8,10,17,39,43,46}$, for the three rheology models.

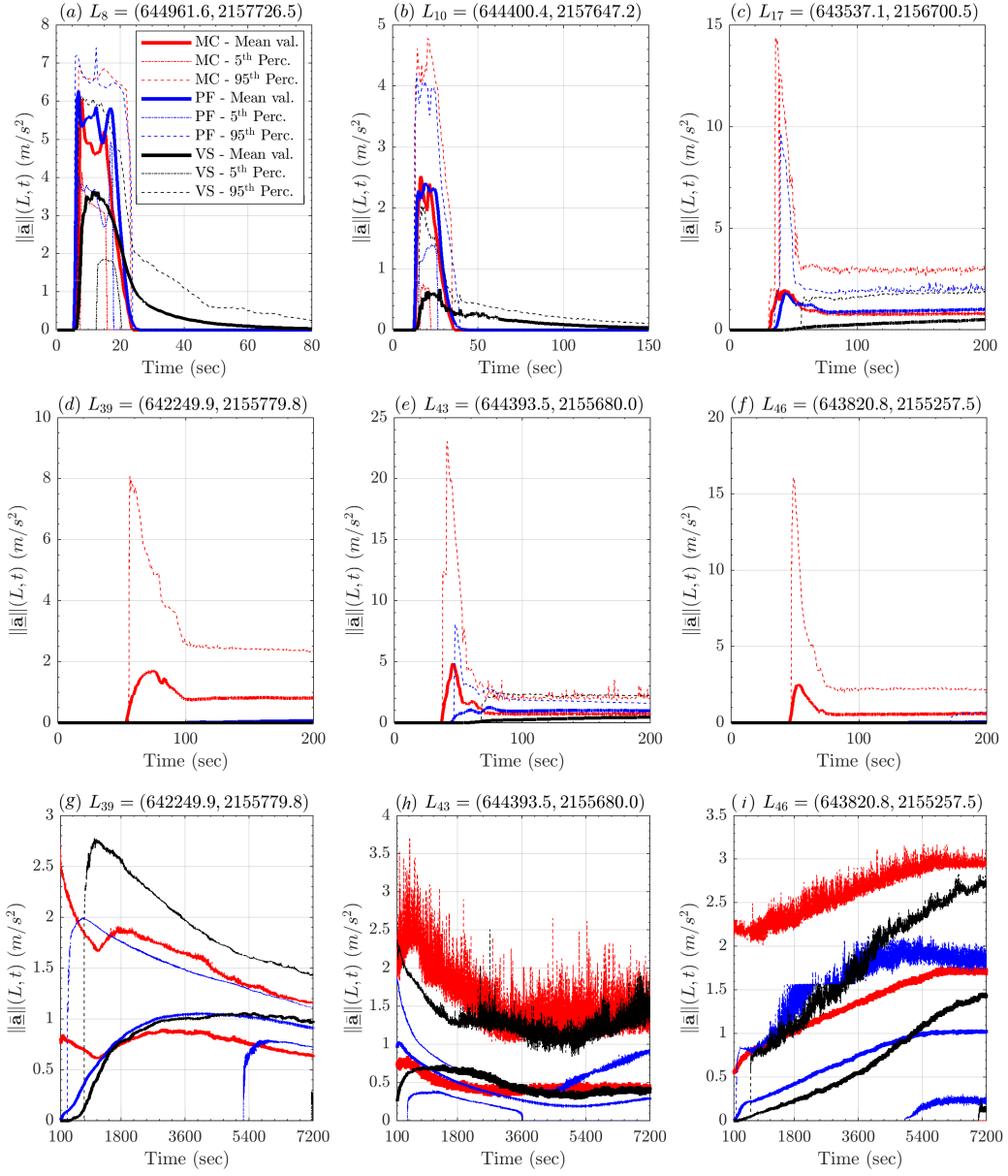


Figure 21: Records of flow acceleration magnitude (computed from LHS), in six selected locations. Records of points L_{39} , L_{43} , and L_{46} are displayed at two different scales, according to the initial dynamics, in plots (d-f), and the asymptotic dynamics, in plots (g-i). Bold line is mean value, dashed lines are 5th and 95th percentile bounds. Different rheology models are displayed with different colors.

5.2.5 Flow area and spatially averaged measurements

Figure 22 shows the spatial average of speed and Froude Number, for the three rheology models. Moreover, it shows the inundated area of flow, as a function of time.

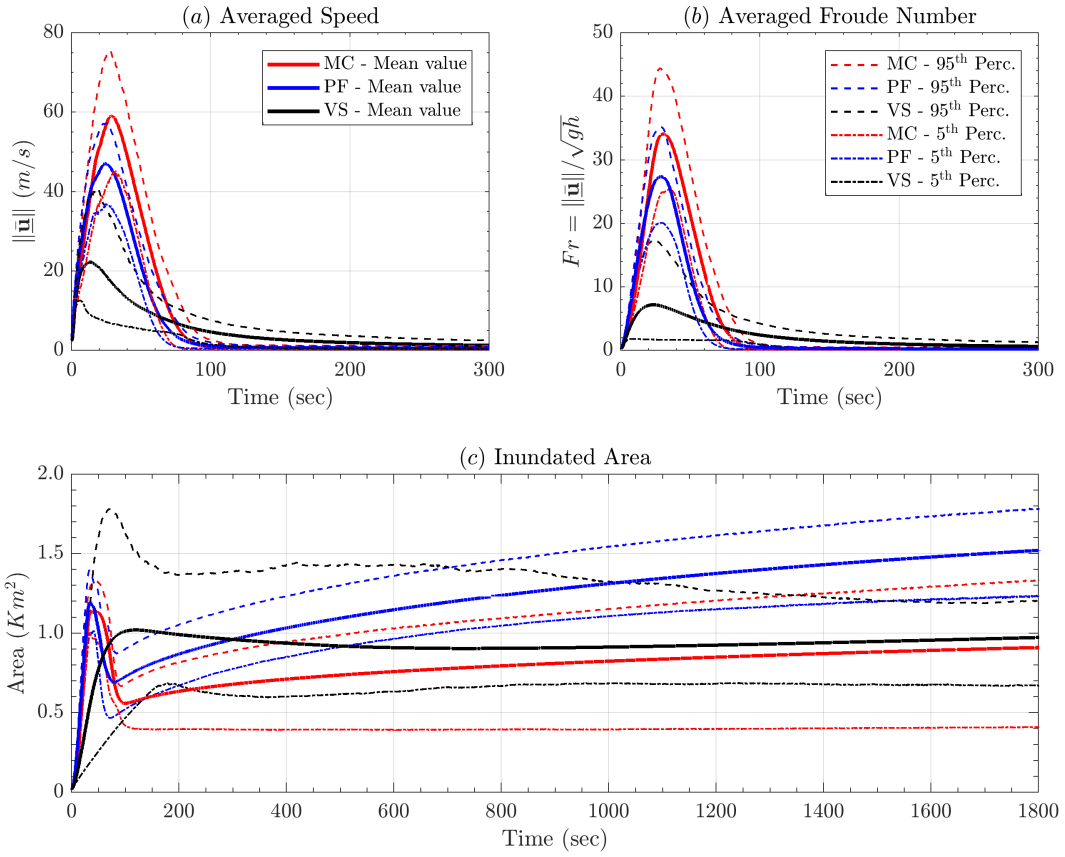


Figure 22: Comparison between spatial averages of (a) flow speed, and (b) Froude Number in addition to the (c) inundated area, as a function of time.

5.3 Hidden dynamic quantities

The current case study does not show a preferential direction, equivalent to the slope direction of the inclined plane. Hence, we will focus on the moduli, and powers, of the force terms detailed in Section 4.2.

5.3.1 Forces, spatial average

Figure 23 shows the spatial average of force terms moduli, for the three rheology models.

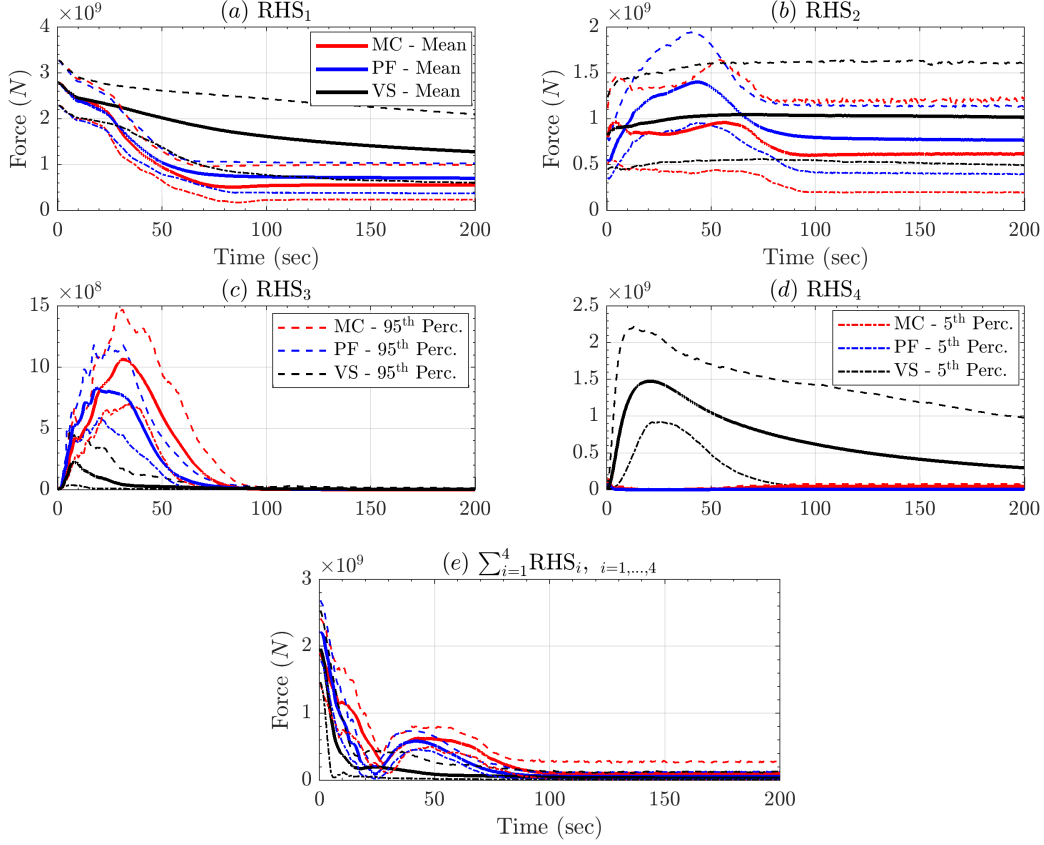


Figure 23: Spatial average of the RHS force terms moduli. Bold line is mean value, dashed lines are 5th and 95th percentile bounds.

5.3.2 Powers, spatial average

Figure 24 shows the spatial average of powers, for the three rheology models.

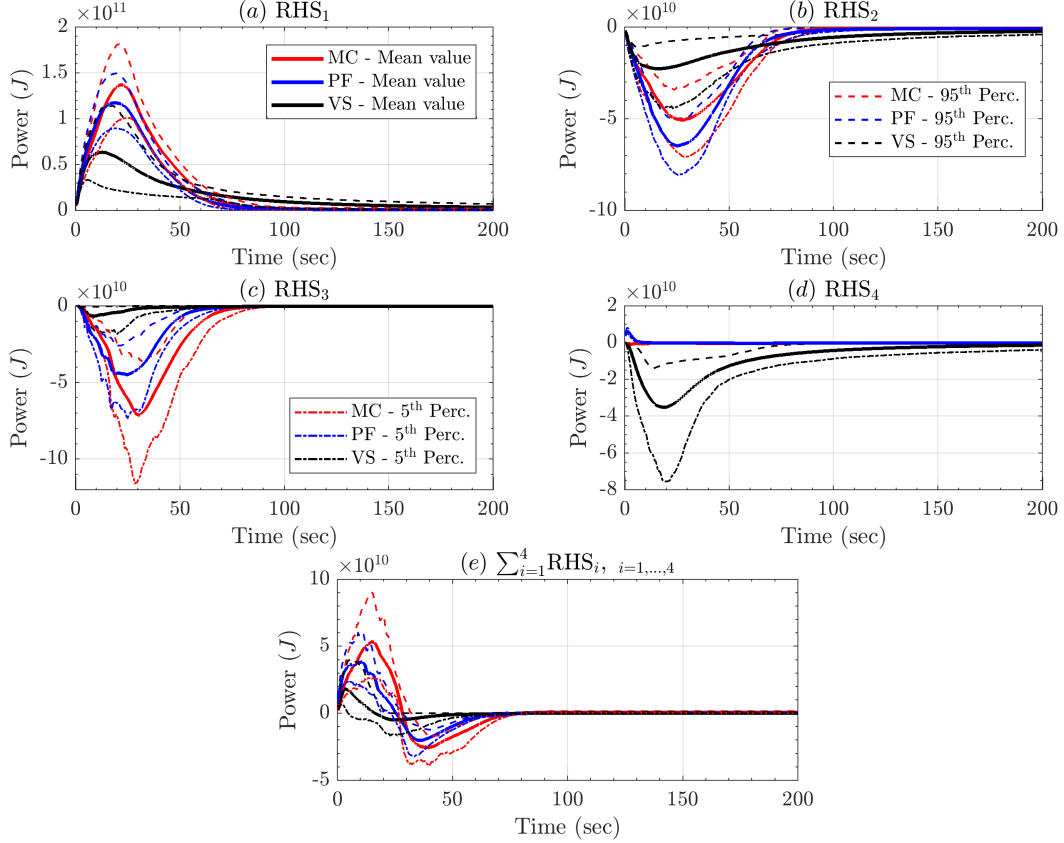


Figure 24: Spatial average of the RHS powers. Bold line is mean value, dashed lines are 5th and 95th percentile bounds. Model comparison on the mean value is also displayed.

5.3.3 Force contribution coefficients, RHS terms

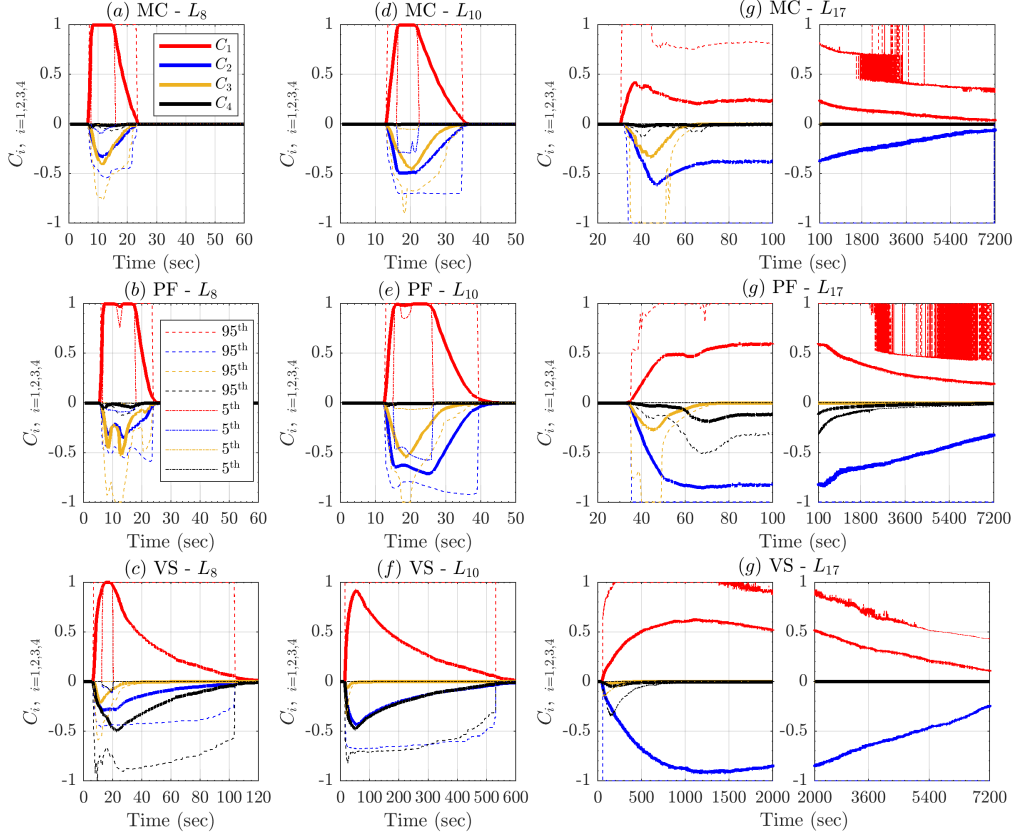


Figure 25: Records of contribution coefficients of **RHS** forces, in the slope direction, at four spatial locations of interest. Bold line is mean value, dashed/dotted lines are 5th and 95th percentile bounds. Different rheology models are displayed with different colors. Dominant factor is calculated based on the l^∞ norm (see Section 3.1)

5.3.4 Force dominance factors, RHS terms

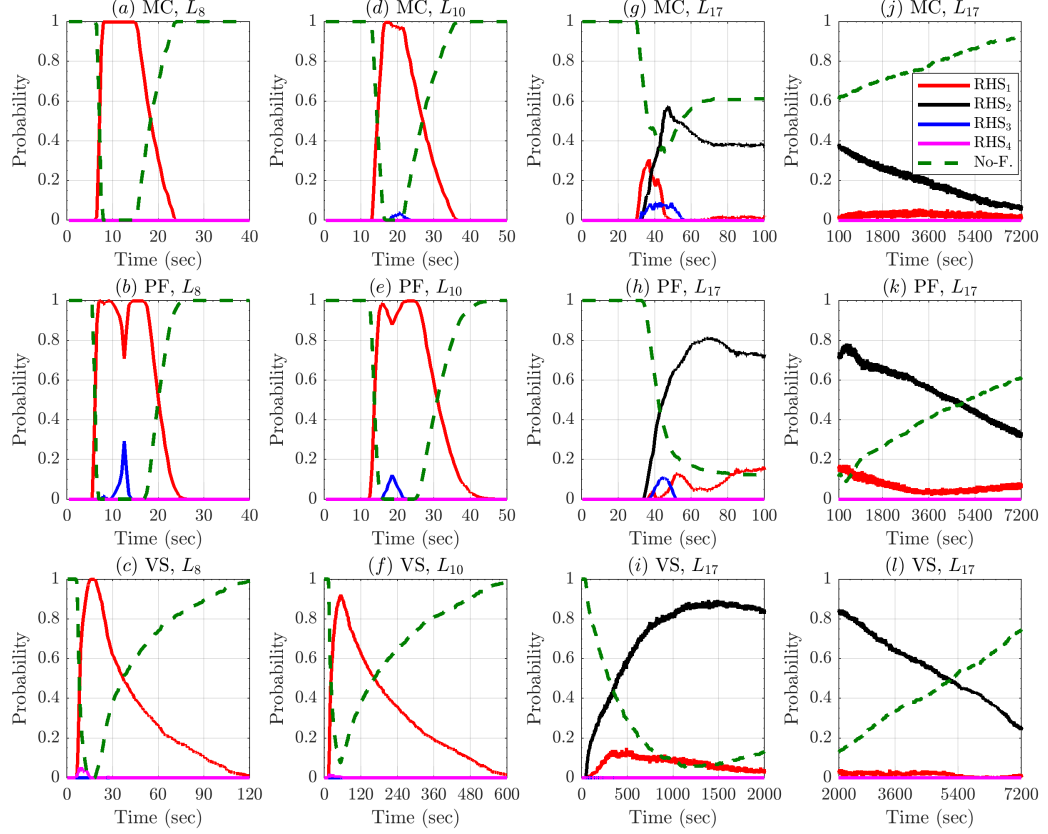


Figure 26: Records of dominance probabilities of **RHS** forces, in the slope direction, at four spatial locations of interest. Bold line is mean value, dashed/dotted lines are 5th and 95th percentile bounds. Different rheology models are displayed with different colors. No-flow probability is also displayed.

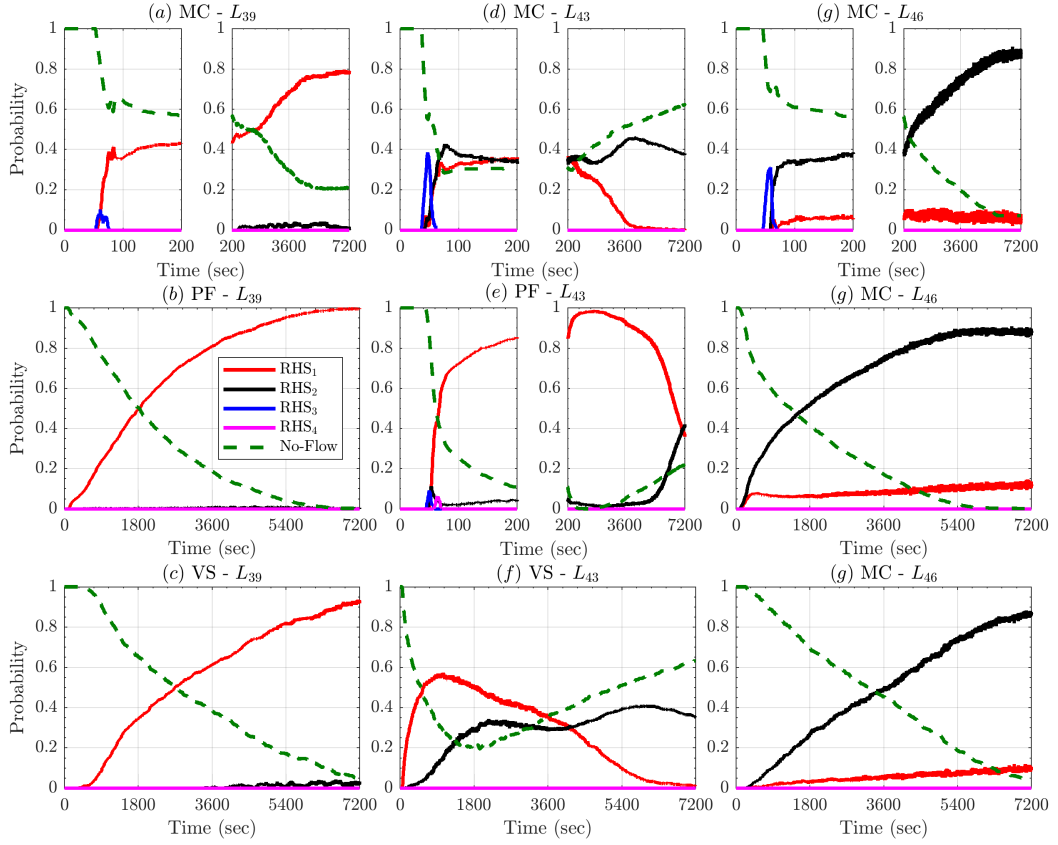


Figure 27: Records of dominance probabilities of **RHS** forces, in the slope direction, at four spatial locations of interest. Bold line is mean value, dashed/dotted lines are 5th and 95th percentile bounds. Different rheology models are displayed with different colors. No-flow probability is also displayed.

6 Discussion

Appendix A: Latin Hypercubes and orthogonal arrays

The Latin Hypercube Sampling (LHS) is a well established procedure for defining pseudo-random designs of samples in \mathbb{R}^d , with good properties with respect to the uniform probability distribution on an hypercube $[0, 1]^d$ (?????). In particular, compared to a random sampling, a LHS: (i) enhances the capability to fill the d-dimensional space with a finite number of points, (ii) in case $d > 1$, avoids the overlapping of point locations in the one dimensional projections, (iii) reduces the dependence of the number of points necessary on the dimensionality d .

Definition 5 (Latin hypercube sampling) Let $\Xi = \{\xi_i : i = 1, \dots, N\}$ be a set of points inside the d -dimensional hypercube $C = [0, 1]^d$. Let $[0, 1] = \bigcup_{j=1}^N I_j$, where $I_j = [\frac{(j-1)}{N}, \frac{j}{N}]$. Let $\xi_i = (\xi_i^1, \dots, \xi_i^d)$, and for each $k \in \{1, \dots, d\}$, let $\Xi^k = \{\xi_i^k : i = 1, \dots, N\}$. Let λ^d be the uniform probability measure supported inside C , called Lebesgue measure. Then Ξ is a latin hypercube w.r.t. $\lambda^d \iff \forall j \in \{1, \dots, N\}, \forall k \in \{1, \dots, d\}, |I_j \cap \Xi^k| = 1$.

The procedure is simple: once the desired number of samples $N \in \mathbb{N}$ is selected, and $[0, 1]$ is divided in N equal bins, then each bin will contain one and only one projection of the samples over every coordinate.

The LHS definition is trivially generalized over $C = \prod_i^d [a_i, b_i]$, i.e. the cartesian product of d arbitrary intervals. That will be applied in this study, defining LHS over the parameter domain of the flow models.

There are a large number of possible designs, corresponding the number of permutations of the bins in the d -projections, i.e. $d \cdot N!$. If the permutations are randomly sampled there is a high possibility that the design will have good properties. However, this is not assured, and clusters of points or regions of void space may be observed in C . For this reason, we base our design on the orthogonal arrays (OA) (??).

Definition 6 (Orthogonal arrays) Let $S = \{1, \dots, s\}$, where $s \geq 2$. Let $Q \in S^{n \times m}$ be a matrix of such integer values. Then Q is called an $OA(n, m, s, r) \iff$ each $n \times r$ submatrix of Q contains all possible $1 \times r$ row vectors with the same frequency $\lambda = n/s^r$, which is called the index of the array. In particular, r is called the strength, n the size, ($m \geq r$) the constraints, and s the levels of the array.

Orthogonal arrays are very useful for defining latin hypercubes which are also forced to fill the space (or its r -dimensional subspaces) in a more robust way, at the cost of potentially requiring a larger number of points than a traditional LHS.

Proposition 7 Let Q be an $OA(n, m, s, r)$. Then let $U \in \mathbb{R}^{n \times m}$ be defined as follows:

$$\forall k \in \{1, \dots, s\}, \forall j \in \{1, \dots, m\}, \{Q[\cdot, j] : Q[i, j] = k\} = \Pi(\{(k-1)\lambda s^{r-1}, \dots, k\lambda s^{r-1}\}),$$

where Π is a random permutation of λs^{r-1} elements. Then $\Xi = \{\xi_i = U[i, \cdot] : i = 1, \dots, n\}$ is a LHS w.r.t to λ^m over $C = [0, 1]^m$. Moreover, let $[0, 1]^r = \bigcup_{(h_1, \dots, h_r)=1}^s I_{(h_i)}$, where $I_{(h_i)} = \prod_{i=1}^r [\frac{(h_i-1)}{s}, \frac{h_i}{s}]$. Then $\forall D = (d_1, \dots, d_r) \subseteq \{1, \dots, m\}$, let $\Xi^D = \{(\xi^{d_1}, \dots, \xi^{d_r}) : i = 1, \dots, n\}$. We have that

$$\forall k \in \{1, \dots, s\}, \forall (h_i : i = 1, \dots, r) \in \{1, \dots, d\}^r, |I_{(k_i)} \cap \Xi^D| = \lambda.$$

For each column of Q we are replacing the λs^{r-1} elements with entry k by a random permutation of $((k-1)\lambda s^{r-1} + h)_{h \in 1, \dots, \lambda s^{r-1}}$. After the replacement procedure is done, the newly obtained matrix U is equivalent to a LHS which inherits from Q the property of fully covering s^r equal r -dimensional hypercubes in every r -dimensional projection. Each hypercube contains λ points. In other words, inside each r -dimensional projection, the design associated to U fills the space like a regular grid at the scale of those s^r hypercubes, but it is still an LHS at a finer scale, i.e. the λs^{r-1} one dimensional bins. A complete proof can be found in ? and it is a straightforward verification of the required properties.

However, even in an LHS based on an $OA(n, m, s, r)$, if $r < m$ what happens in the projections with dimension $r' > r$ is not controlled, and randomizing procedures are made more difficult by the additional structure imposed by the OA. Moreover, the total number of points necessary to achieve a full design increases with r , and hence is affected by dimensionality issues.

Dealing with relatively small d , i.e. $d \in \{3, 4\}$, we adopt a LHS U created by a $OA(s^d, d, s, d)$. The strength is equal to the dimension d , hence the design fills the entire space like a d dimensional grid, but it is a LHS as well. In this case there is one point in each hypercube, and $\lambda = 1$. We take $s = 8$ for the 3-dimensional designs over the parameter space of Mohr-Coulomb and Voellmy-Salm models, i.e. 512 points; we took $s = 6$ for the 4-dimensional designs over the more complex parameter space of the Pouliquen-Forterre model, i.e. 1296 points.